

# PIV measurements of water mist transport in a homogeneous turbulent flow past an obstacle

Cary Presser<sup>a,\*</sup>, George Papadopoulos<sup>b</sup>, John F. Widmann<sup>c</sup>

<sup>a</sup>National Institute of Standards and Technology, 100 Bureau Drive, Stop 8360, Gaithersburg, MD 20899-8360, USA

<sup>b</sup>ATK GASL, 77 Raynor Avenue, Ronkonkoma, NY 11779, USA

<sup>c</sup>Fluent Inc., 10 Cavendish Court, Lebanon, NH 03766, USA

Received 26 August 2005; received in revised form 20 April 2006; accepted 30 May 2006

Available online 11 September 2006

## Abstract

To obtain a better understanding of the physical processes involved in liquid suppressant transport in cluttered spaces, particle image velocimetry (PIV) measurements were carried out in the droplet-laden, grid-generated, homogeneous turbulent flow over both an unheated and heated cylinder, and a body-centered cube (BCC) arrangement of spheres. Transport of both water droplets and aerosol particles was characterized upstream and downstream of these obstacles. Data were recorded for the cylinder at ambient and elevated temperatures (at 423 K) to estimate the effects of the hot cylinder surface on droplet transport. The results indicated that smaller droplets are entrained into the recirculation region behind the cylinder while the larger droplets impact the cylinder surface, accumulate and drip off, and/or rebound off the surface and disperse into the free stream. The flow over the heated cylinder resulted in the formation of a vapor layer on the downstream side of the cylinder in the shear region between the recirculation zone and free stream. Thus, vaporization of larger droplets impinging on the heated cylinder surface suggests an increased probability of vapor. For the BCC (with a blockage ratio of about 64%), there was both transport of droplets and seed particles around and through the BCC, as well as significantly more liquid accumulation and dripping than for the cylinder.

Published by Elsevier Ltd.

**Keywords:** Droplet-laden flows; Droplet transport; Fire suppression; Grid-generated turbulence; Heated cylinder; High boiling point suppressants; Homogeneous turbulent flow; Obstructed spaces; Particle image velocimetry; Spray impingement

## 1. Introduction

Fires within an aircraft engine nacelle pose significant challenges for suppression owing to the presence of wires, fuel, hydraulic, and electrical lines, ribs and other objects (e.g. mounting brackets), which can obstruct transport of a suppression agent to the fire source (e.g. broken fuel line). The complex arrangement of components inside an aircraft engine nacelle creates an environment for spray transport that is characterized by a high degree of turbulence, high blockage ratios, and significant liquid impingement onto surfaces. Non-ozone-depleting halogen alternatives developed for such applications include chemical suppressants that have high boiling point temperatures ( $T_b > 330$  K), and

exist in the liquid phase after high-pressure release and under ambient conditions. Liquid suppressants are of particular interest because of their higher absorption of heat per unit volume, compared to gaseous suppressants, which results in a greater reduction of flame and surface temperatures, as well as their ease of storage which is important for aerospace applications [1]. Release of these agents in a confined, cluttered space results in the dispersal of droplets that may impact upon solid surfaces and reduce the fire suppression effectiveness of the agent. For this investigation, a droplet-laden, homogeneous turbulent flow field was used to simulate the turbulence experienced by sprays for a representative fire-suppression scenario in an aircraft engine nacelle at reported airflow conditions [2]. The choice of the above conditions was motivated by recent efforts to develop and validate the subgrid droplet impact model of the VULCAN computational fluid

\*Corresponding author. Tel.: +1 301 975 2612; fax: +1 301 869 5924.

E-mail address: [cpresser@nist.gov](mailto:cpresser@nist.gov) (C. Presser).

**Nomenclature**

$k_t$	total turbulence kinetic energy
$n$	number of samples
$N$	total number of velocity vectors
$s$	standard deviation of the mean
$T_i$	local mean turbulence intensity
$U$	spanwise (across the cylinder) out-of-plane component of velocity
$V$	cross-stream component of velocity
$W$	streamwise component of velocity
$W_0$	nominal streamwise velocity
$U_i$ ( $= U, V, W$ )	mean of the components of the individual velocity vectors
$u_i$ ( $= u, v, w$ )	components of the individual velocity vectors
$U_i U_j$ ( $= UV, UW, VW$ )	components of the velocity correlation coefficients

$u_c$	combined standard uncertainty
$\Delta x, \Delta y, \Delta z$	true particle displacements
$Z$	streamwise position

*Greek symbols*

$\Delta\chi, \Delta\eta$	pair of two-dimensional displacements
$\varepsilon(U), \varepsilon(V), \varepsilon(W)$	calibration uncertainties for the three components of velocity
$\rho_{ij}$	velocity correlation coefficients
$\sigma_i$	root mean square of the fluctuating components of velocity

*Subscripts*

$i = U, V, W$	index for the components of velocity
$ij = UV, UW, VW$	index for the velocity correlation coefficients

dynamics (CFD) fire physics code for spray-clutter interactive environments [3].

A large body of literature exists on specific segments of the problem investigated here, however, there are few investigations that address the full complexity of the problem. For example, literature exists for specific issues related to grid-generated turbulence, droplet transport in vortices, and droplet/spray impingement on surfaces. Past research includes single isolated droplet impingement on flat surfaces (e.g. Ref. [4]) and cylinders (e.g. Ref. [5]), dripping liquid droplets off cylinders (e.g. Ref. [6,7]), spray impingement on unheated and heated flat surfaces in different boiling regimes (e.g. Refs. [8–10]), droplet interactions with shear layers (e.g. Ref. [11]), and droplet entrainment in free turbulent flows (without impingement) to determine the influence of the flow on droplet trajectories (e.g. Ref. [12]).

Regarding quantitative measurements for validating multiphase CFD codes, particle image velocimetry (PIV) is a diagnostic method that has been used extensively in fluid flow characterization, and has recently attracted attention for spray characterization. PIV has been used to obtain two-dimensional spatial maps of the three components of velocity, as well as turbulence information such as Reynolds stresses, in a variety of fluid dynamic studies over different body configurations. Several PIV studies of sprays have dealt with fire and combustion applications (e.g. Refs. [13–15]), and direct injection and diesel engines (e.g. Refs. [16–20]) in which one can either measure the droplet velocity field, or introduce seed particles (assumed to follow the fluid stream) to the spray field and try to segregate between the continuous and discrete phases. Fire examples include Gorman and Widmann [21] who used PIV to characterize the velocity field in a residential fire sprinkler water spray. They observed that the polydispersity of the droplet sizes has

an effect on the measured velocity field. Widmann et al. [22] compared the droplet velocity measurements obtained in a water spray produced by a residential fire sprinkler using PIV with those obtained using phase Doppler interferometry. The data showed good agreement between the two measurement techniques in regions of the spray where the droplet size distribution was heavily weighted towards the larger droplets. Along the sprinkler axis, however, there was significant disagreement between the two methods. This was attributed to several factors, including possible biasing of the PIV measurements towards the velocities of the larger droplets. Sheppard et al. [23,24] measured the mean velocity field of the water sprays produced by fire sprinklers using PIV. The data were used to provide input for the Fire Dynamics Simulator, a large eddy simulation model developed at the National Institute of Standards and Technology to predict the dynamics of large-scale fires [25]. The data of Sheppard and Lueptow [26] and Sheppard [27] provide the necessary input required to simulate the interaction of fires and water sprays.

The focus of this effort is to investigate the dispersal of liquid fire suppression agents around solid obstacles, and obtain a better understanding of the physical processes of droplet transport in cluttered spaces. Baseline PIV measurements of the gas and droplet phase velocities with and without obstacles were carried out to study droplet dispersion of a liquid agent around cylinders, the cylinder representing the classical obstruction to be modeled. The cylinder diameters were chosen to be smaller than, similar to, and larger than the characteristic length scale of turbulence, which would allow investigation of the effects of turbulence intensity on clutter size. Also, PIV measurements were obtained of the discrete (spray) and continuous (gas) phase velocities for two representative obstacles—a cylinder (of diameter larger than the characteristic length-scale of

turbulence), and a body-centered cubic arrangement of spheres. The cylinder represents a classical configuration and the body-centered cube represents a more complicated scenario. The cylinder was also heated to explore thermal effects on droplet vaporization and transport around the cylinder.

## 2. Experimental arrangement

The experimental arrangement was designed to provide a well-characterized, homogeneous turbulent flow field around prescribed obstacles. Two experimental configurations were used in this investigation. The first was a vertical arrangement in which PIV measurements were carried out for only the gas-phase turbulent flow field. The PIV measurements were also carried out in a second horizontal arrangement in which the flow field was laden with water droplets.

### 2.1. Vertical configuration

For the vertical configuration, an octagon-shaped, clear plastic enclosure (with a wall thickness of 6 mm, height of 610 mm, and major and minor axes of 760 and 560 mm for the cross section, respectively) was used to define the boundary conditions (see Fig. 1). A honeycomb layer was used to laminarize the airflow. The honeycomb was 51 mm thick with approximately 3 mm (length between opposite sides) hexagon-shaped cells. A layer of wire mesh screen (3.2 mm wire thickness and 13 mm size cells) was placed downstream of the honeycomb to impose grid-generated turbulence on the air stream. The incoming air was directed entirely through a selected 125 mm × 254 mm rectangular cross-sectional portion of the honeycomb and then through the wire mesh screen (placed 25 mm downstream of the honeycomb), as shown in Fig. 2. The incoming air was

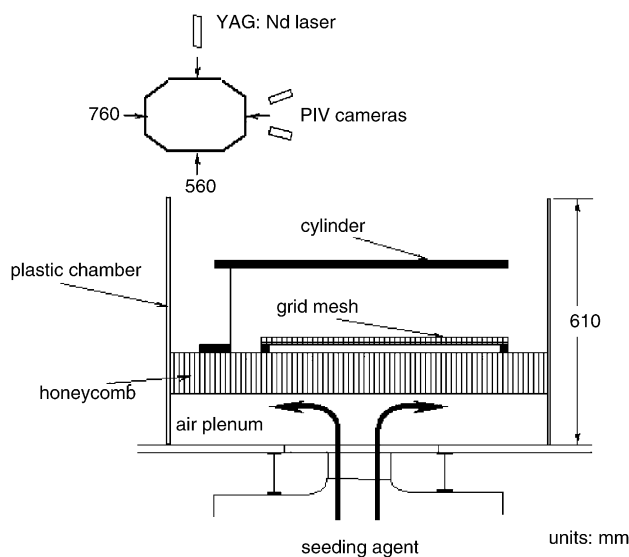


Fig. 1. Schematic of the experimental vertical arrangement for the grid-generated turbulent flow field.

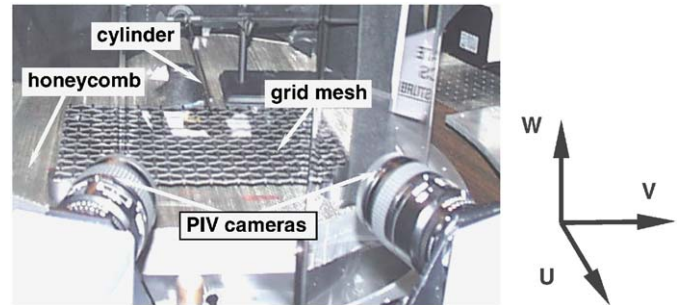


Fig. 2. View of the experimental vertical arrangement with cameras from the PIV system in the foreground.

adjusted to provide droplet mean velocities of about 4–5 m/s near the cylinder. Three cylinders with diameters of 3, 13, and 32 mm, were chosen to span ranges of clutter sizes smaller than, on the same order of, and larger than the integral length scales of turbulence. The obstacles were placed 100 mm downstream of the honeycomb. Placement of the grid mesh and obstacles were chosen to be downstream of any jetting of the airflow from the honeycomb and grid mesh, respectively, as will be discussed further in detail. A stepper-motor-driven traversing system was used to translate the entire assembly and permit measurement of the flow field characteristics at selected locations around the obstacle. The PIV system was aligned around the plastic enclosure (see Fig. 2) with the laser sheet traversing normal to the cylinder, and independent of the traverse.

### 2.2. Horizontal configuration

For the horizontal configuration, the plastic enclosure was placed on its side and, along with a front face that supported the inlet passages for the liquid agent and air, and a back face that supported the exhaust passage, served to form a closed system at room temperature. The experiment was oriented horizontally to enable collection of liquid agent that dripped off of the obstacle, and prevent liquid droplets downstream of the obstacle from falling back upstream into the oncoming stream. The agent used in this study was water, which was supplied to the flow field by means of a 60° hollow-cone, pressure-jet atomizer (with a nominal flow rate of 3.78 kg/h). For these experiments, the water spray with coflowing air was introduced to the grid-generated turbulent flow field. The largest of the three aforementioned cylinders, which was modified to include a cartridge heater for preheating of the cylinder, served as the obstacle towards which the water spray was directed. The incoming air (supplied at  $440 \pm 0.12 \text{ kg/h}^1$ ) was directed

<sup>1</sup>Estimation of the measurement uncertainty is determined from statistical analysis of a series of replicated measurements (referred to as Type A evaluation of uncertainty), and from other means other than statistical analysis (referred to as Type B evaluation of uncertainty) [28]. Calculated as  $2u_c$  (representing a level of confidence of 95%), where  $u_c$  is the combined standard uncertainty. The value for  $u_c$  was estimated statistically by  $sn^{-1/2}$ , where  $s$  is the standard deviation of the mean and  $n$

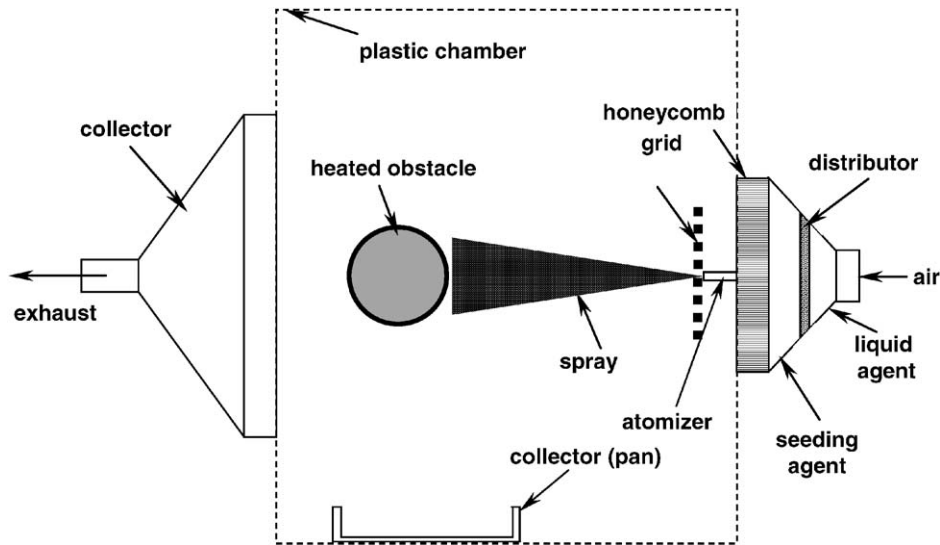


Fig. 3. Schematic of the experimental horizontal arrangement for the droplet-laden, grid-generated turbulent flow field.

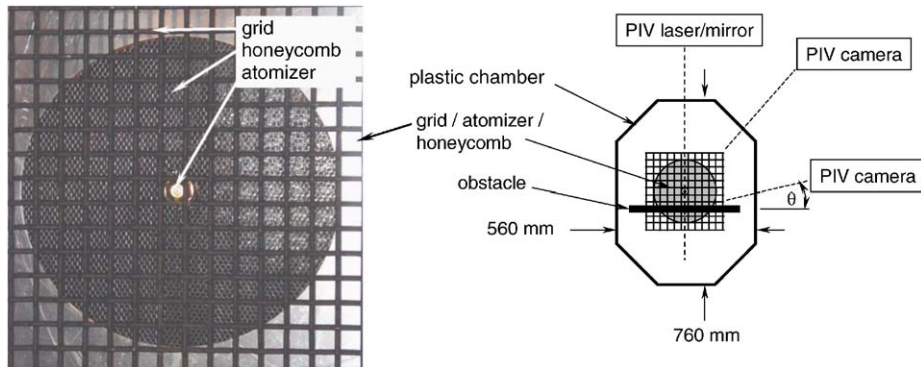


Fig. 4. Upstream view and schematic of the inlet for the experimental horizontal configuration, and orientation of the particle image velocimeter (PIV) with respect to the heated cylinder.

entirely through a distributor plate with steel wool, a circular cross-sectional area of honeycomb, and then through a wire mesh screen, as illustrated in Fig. 3. The honeycomb had a 203 mm outer diameter (i.e. exposed to the downstream flow). The honeycomb and wire mesh screen were co-positioned around the atomizer (having a diameter of 17.8 mm), which resulted in removal of the central portion of the honeycomb (of an approximate area of  $521.9 \pm 0.19 \text{ mm}^2$ ). The mean of the inlet air velocity was estimated by multiplying the honeycomb cell area by the approximated number of cells (3333 cells) exposed to the downstream flow field.

Grid-generated turbulence was imposed on the air stream by placing a square layer of wire mesh screen (with dimensions of 229 mm width by 330 mm length, 3.2 mm wire thickness, and 13 mm size cells) 25 mm downstream of the honeycomb. Note that the grid mesh covered the entire inlet area (compare the aforementioned honeycomb

diameter to the grid dimensions). A schematic of the grid mesh pattern relative to the atomizer and incoming airflow is shown in Fig. 4. The face of the liquid atomizer was placed flush with the upstream side of the grid mesh, and centered within one mesh cell so that the liquid spray would be unimpeded by the grid mesh. Again, the stepper-motor-driven traversing system translated the entire experimental assembly, while the PIV system was aligned at a stationary location, and independent of the traverse (see Fig. 5).

Measurements were carried out with two obstacles, an aluminum cylinder and a body-centered cube (BCC) arrangement of wooden spheres and connecting posts (see Figs. 6 and 7, respectively). The cylinder, which was chosen because its diameter is larger than the integral length scale of turbulence, was fabricated from a solid aluminum rod, with an outer diameter of  $32 \pm 0.04 \text{ mm}$  and length of 305 mm (see Fig. 6). Note that the cylinder had a length that did not span across the entire cross section of the chamber (to easily adjust its position relative to the spray nozzle), and a spanwise flow existed along the cylinder length due to end effects. The spray impinged

(footnote continued)

is the number of samples (Type A uncertainty, where  $n = 11$ ), and from the manufacturer uncertainty (Type B uncertainty), if available.

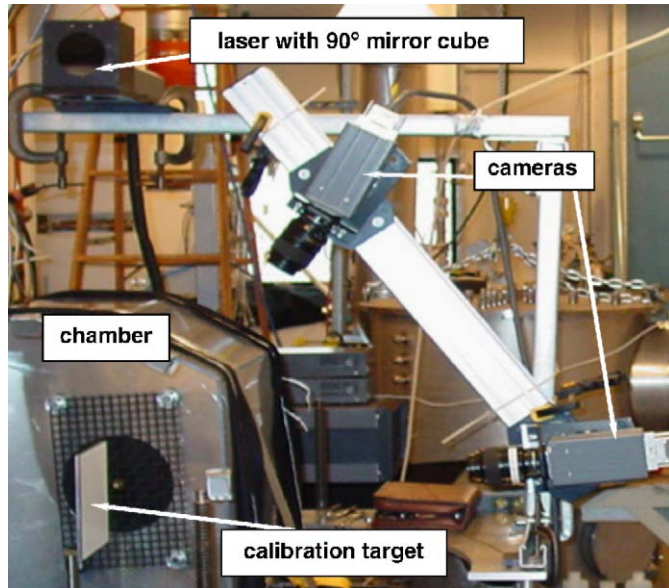


Fig. 5. View of the experimental horizontal configuration with the cameras and laser for the PIV system.

along the central portion of the cylinder and was estimated to cover up to approximately 183 mm of the cylinder's upstream surface (taking into account the aforementioned spray angle, cylinder diameter, and atomizer/cylinder distance). This impingement region was well away from the cylinder edges. Entrainment of the droplets with the airflow also reduced the dispersion of the spray. Thus, we confined our measurements to along the center plane to minimize any related edge effects. Surface heating was provided by a 13 mm diameter hole bored through the center of the cylinder to accommodate a 250 W cartridge heater (13 mm in diameter and 76 mm in length). The rod was split along its axis into two halves to allow 1 mm deep channels to be milled along one segment for placement of five K-type thermocouples (Inconel sheathed, ungrounded, 0.8 mm in diameter, and 305 mm in length). The thermocouple time response, as specified by the manufacturer was 3 s at a level of confidence of 95%. The cylinder halves were bolted together and re-machined to produce a seamless outer diameter. The thermocouples were placed in a cross pattern (see Fig. 6) in the center of the rod (each separated by a distance along the surface of 6.4 mm, with the thermocouple junctions placed about 3.2 mm of the surface from within bored holes at each location). The central thermocouple was used for temperature control of the heater, which was positioned behind the thermocouples. The expanded uncertainty for the temperature was 7.9 K, including the Type B uncertainty of 3.1 K. The center of the cylinder was fixed at a location  $185 \pm 4$  mm downstream of the grid mesh. Note that the far-most upstream position from the cylinder where data were obtained was 50.8 mm, which was about 134 mm downstream of the grid mesh. At this relatively large distance, heat transfer from the hot cylinder surface did not influence the initial experimental conditions [29].

The BCC was composed of nine wooden spheres with a nominal diameter of 28 mm, all interconnected with posts (with a nominal length of 24 mm and width of 3.2 mm), as shown in Fig. 7. As with the cylinder, the central sphere of the BCC was aligned with the atomizer. The posts connecting the center sphere were nominally 17 mm in length. The blockage ratio, or obstructed cross-sectional area for an equivalent area encompassing a face of the BCC, was about 64%. The two obstacles were coated with flat black paint to reduce reflections of laser light off their surfaces during the optical measurements. The obstacles were placed nominally 182 mm downstream of the honeycomb, and located along the atomizer centerline.

### 2.3. Particle image velocimetry

#### 2.3.1. PIV measurement system

The flow field upstream and downstream of the different obstacles was characterized using a three-dimensional PIV system manufactured by Dantec Dynamics<sup>2</sup> (see Fig. 5). Particle image velocimetry is a non-intrusive field measuring technique (as opposed to a single-point diagnostic method) that measures two or three components of velocity. The 3D stereo PIV system differs from traditional PIV systems in that two charged-coupled device (CCD) cameras are used, and three velocity components are measured [30]. Special camera mounts were utilized to permit the rotation of the camera body with respect to the camera lens so that the Scheimpflug condition was satisfied, permitting the laser sheet to be in focus despite the non-orthogonal camera alignment [30]. The PIV system consisted of a dual-cavity, 50 mJ Nd:YAG mini-laser as the illumination source (with a pulse duration of the laser light sheet of about 5 ns at a wavelength of 532 nm), two 12 bit  $1024 \text{ pixels} \times 1280 \text{ pixel}$  dual-frame CCD cameras, a data acquisition and control unit, and software running on a personal computer for system control, data management, and data post-analysis. Detailed information on the PIV system configuration and general performance is provided in Refs. [31–33].

#### 2.3.2. PIV methodology

The basic relationship of displacement divided by time to yield velocity is the fundamental principle of the PIV technique. Although PIV is a non-intrusive measurement technique, it requires tracer particles to be entrained in the flow under investigation, so that displacement information is determined. Hence, PIV measures directly the displacement information of tracer particles, and if these particles are small and follow the flow, the displacement information of these small “seeding” particles can be used to infer

<sup>2</sup>Certain commercial equipment or materials are identified in this publication to specify adequately the experimental procedure. Such identification does not imply recommendation or endorsement by the National Institute of Standards and Technology, nor does it imply that the materials or equipment are necessarily the best available for this purpose.

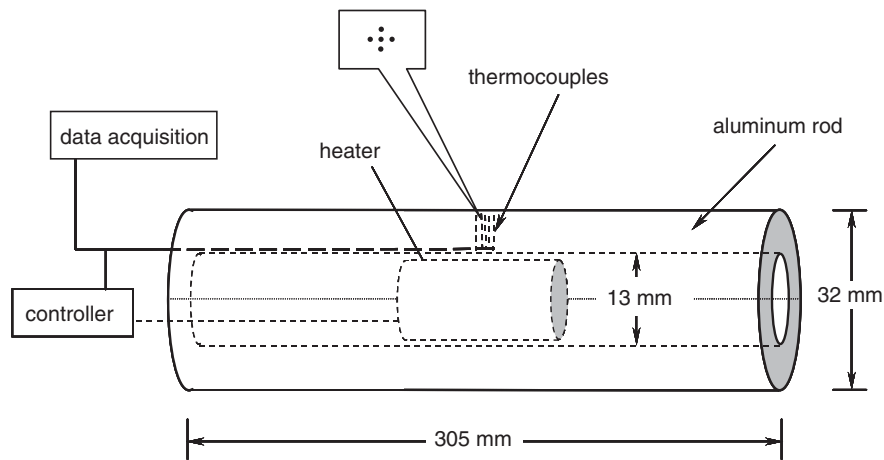


Fig. 6. Schematic of the cylinder with installed cartridge heater. The thermocouples on the upstream side of the cylinder were arranged in the cross pattern shown in the callout.

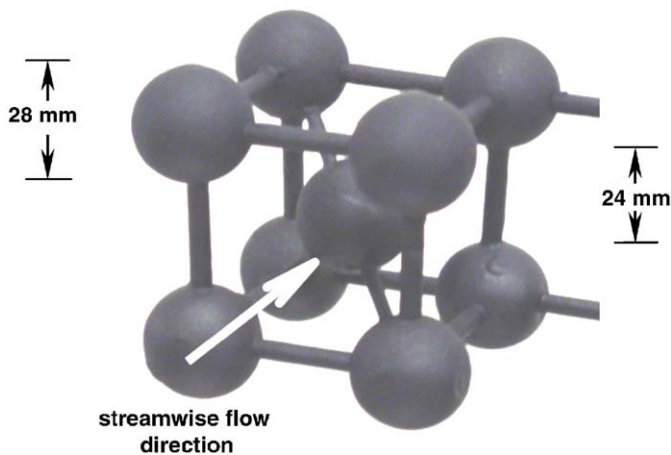


Fig. 7. View of the body-centered cube of spheres.

the flow velocity. On the other hand, the displacement information of droplets, and hence their velocity, is directly measured by the PIV technique.

Illumination of the tracer particles is done using a thin light sheet, which is pulsed to freeze the particle motion. The Mie scattering from the imaged tracer particles is recorded at two instances in time using a digital camera. The two sequential digital images are then sub-sampled at particular areas via a prescribed interrogation window, and a spatial cross-correlation is performed using fast Fourier transform analysis, as described by Willert and Gharib [34], which results in a surface function (e.g. see Fig. 8). The separation time between the light pulses is selected so as to have particles displace several pixels within the interrogation area ( $IA$ ), and have most particles remain common to both images. A high cross-correlation value is determined for which many particle images match up with their corresponding spatially shifted partners, and this is considered to represent the best match of particle images between the sequential recordings.

The displacement vector of the cross-correlation peak from the center (origin) of the two-dimensional interroga-

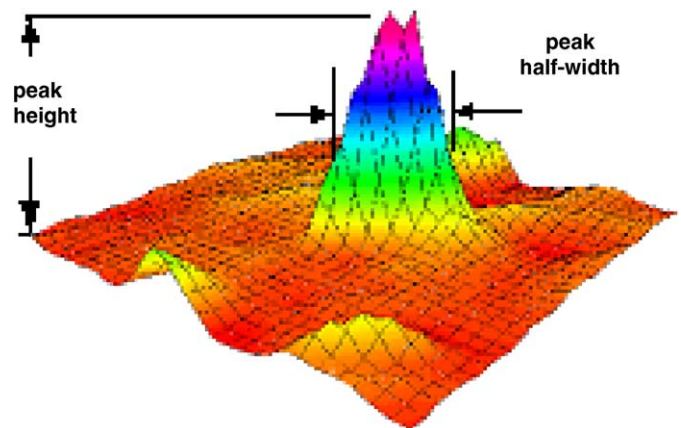


Fig. 8. Typical spatial cross-correlation function between two sequential digital PIV images.

tion window denotes the average distance traveled by the particles within the interrogation area. Accurate estimation of the displacement vector to sub-pixel resolution is performed by locally fitting the two-dimensional array of correlation values in the vicinity of the peak. The absolute displacement vector is then calculated from a calibration of the magnification factor between the pixel domain of the digital recording device and the physical field of view. Finally, division of the displacement vector, determined for each interrogation area along the entire pixel domain, by the time separation between the two sequential laser pulses yields the velocity vector field in the physical area under investigation.

To improve the signal-to-noise ratio and reduce errors in displacement estimation, a multi-pass adaptive correlation technique is used whereby the second interrogation area is displaced dynamically to capture the particle movement while at the same time being reduced in size. In this way, the effective probe volume of the PIV is reduced and stretched to follow along particle path lines, while yielding good spatial resolution along flow gradients. In addition, a further sub-pixel refinement step is used to eliminate the

bias error from the displacement estimation and dramatically reduce the random errors, thus achieving higher accuracy in the PIV signal [35].

Using the above methodology, a planar velocity field is obtained corresponding to the vector projection in the illumination plane. By using two cameras to image the same planar flow field from two separate points of view, one obtains two distinct planar velocity fields. This is the foundation of the stereoscopic PIV principle, as illustrated in Fig. 9. Stereoscopic PIV takes advantage of the parallax error that is inherent in 2D planar PIV measurements, an error that comes about from imaging the projected trajectory of particles in the plane of the laser light sheet, instead of the actual three-dimensional trajectory. By imaging particle displacements from two distinctly different viewing angles, distinct projected trajectories for the same group of particles are determined.

To properly view the plane illuminated by the light sheet using the stereo-PIV arrangement, the camera back plane (i.e. the CCD-chip) must be tilted to properly focus the entire camera field of view. A special optical arrangement is required to meet the so-called Scheimpflug condition, which states that the image, lens, and object plane must be collinear for the camera images to be properly focused in the entire field of view [36].

The two-dimensional projected trajectories are combined using a numerical model that describes how each camera images the flow field to determine the actual three-dimensional trajectory of the group of particles within the laser sheet. The numerical model is determined using a well-defined calibration target that is used to imitate the out-of-plane motion. Placing the target in the actual measurement station offers a robust way of calibrating the system; one that easily takes into account distortions caused by index-of-refraction effects, and thus is the preferred way of calibrating current stereoscopic PIV measurements.

Construction of the three-dimensional velocity map means that true particle displacements ( $\Delta x$ ,  $\Delta y$ ,  $\Delta z$ ) are extracted from a pair of two-dimensional displacements ( $\Delta \chi$ ,  $\Delta \eta$ ) that correspond to the vector results obtained from both cameras. This means that a system of four equations and three unknowns needs to be solved, and depending on the approach, the equations may be linear or non-linear, as discussed in Ref. [37].

Conducting PIV measurements in polydisperse sprays introduces an additional complication when compared to single-phase measurements. When spray droplets are used as the “scatterers” for PIV measurements rather than seed particles, a size bias is introduced. The bias results from the stronger signal by larger droplets, owing to the greater intensity of Mie scattered light from these droplets, as compared to smaller ones. The enhanced scattering leads to biasing in the cross-correlations, weighting the measured mean velocity towards the larger droplets. Gorman and Widmann [21] investigated this effect using Monte Carlo simulations, and concluded that the mean velocity obtained from the cross correlations was weighted by the surface area of the droplets. Thus, the average velocities obtained from multiphase PIV measurements correspond to surface-area-weighted mean velocities.

### 2.3.3. PIV implementation

A photograph of the stereo-PIV setup in the present investigation is shown in Fig. 2 (vertical configuration) and Fig. 5 (horizontal configuration). The double-cavity Nd:YAG laser was mounted above the facility for the horizontal configuration and a 90° mirror cube was used to orient the light sheet vertically from above the plastic chamber and onto a cross section of the obstacle (see Fig. 5). The two cameras were placed at angles of about 70° and 110° (vertical configuration), and 95° and 145° (horizontal configuration), as measured from the forward direction of propagation of the laser sheet. Bandpass filters

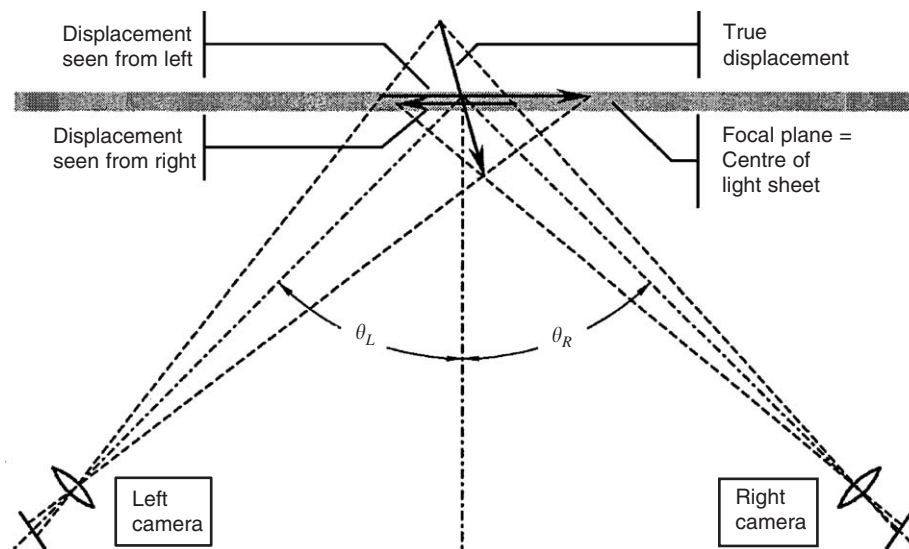


Fig. 9. Principle of stereoscopic PIV (displacement enlarged for better visibility).

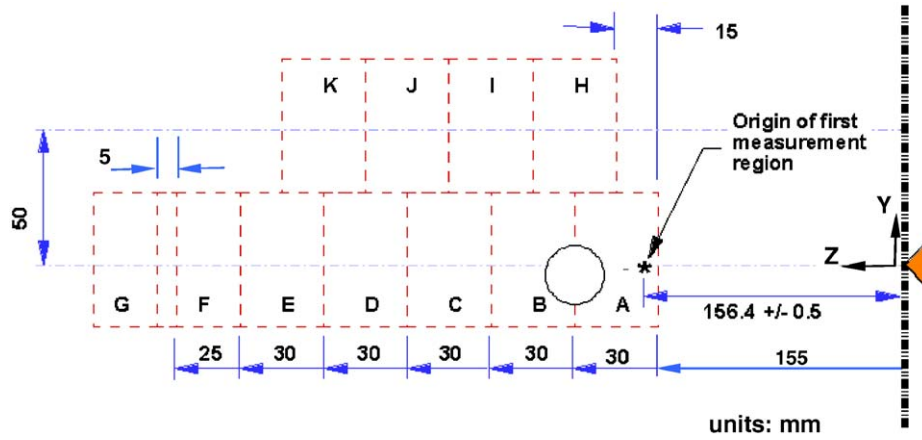


Fig. 10. Schematic of the measurement plane and position of the interrogation areas.

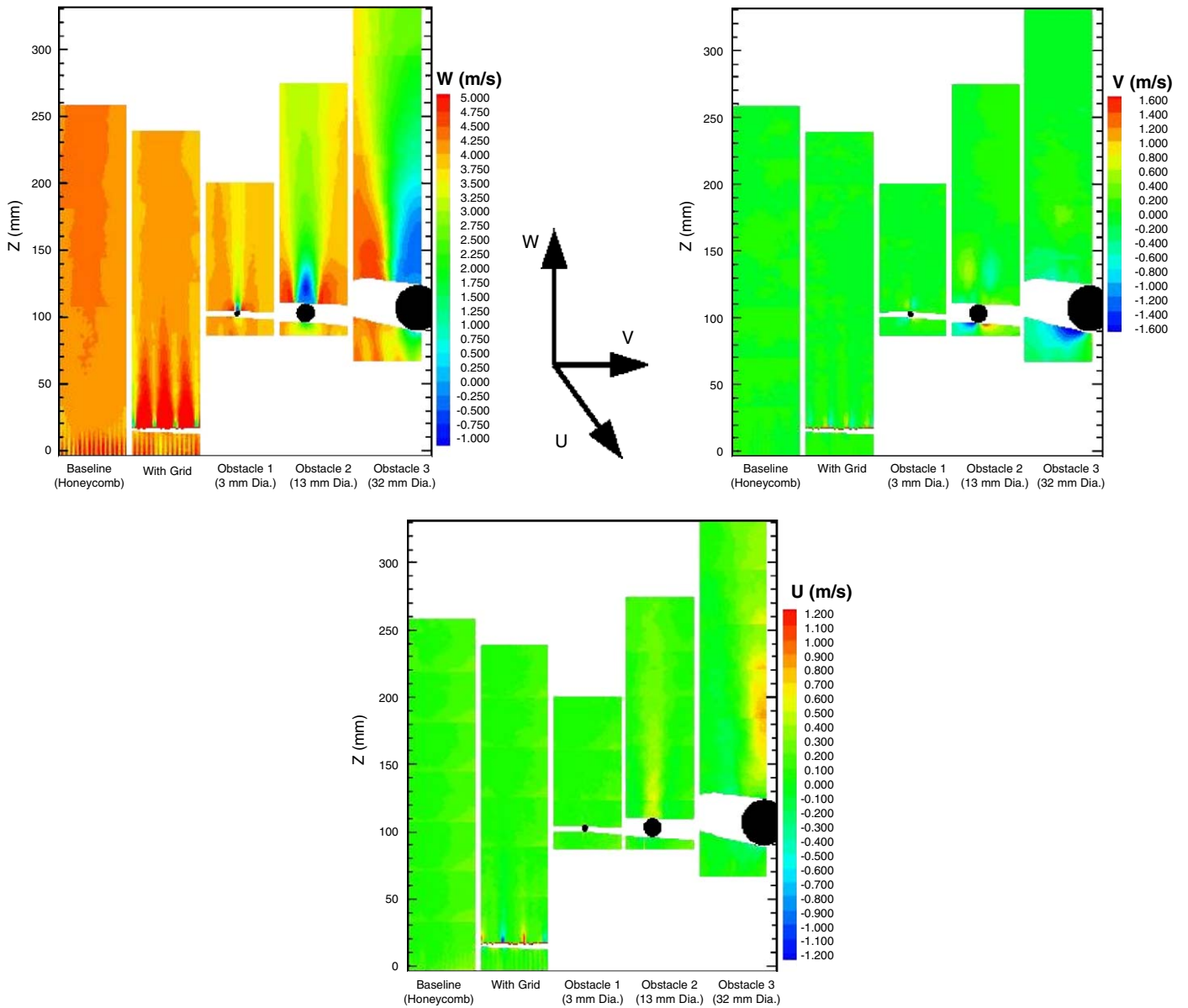


Fig. 11. Variation of mean streamwise ( $W$ ) and cross-stream ( $U, V$ ) velocities with streamwise position ( $Z$ ).

(center wavelength = 532 nm, acceptance window = 30 nm) were used to reject the broadband white light from the room. These filters were mounted in front of Nikon *f*2.8, 105 mm lenses used to image the flow. The processed results are presented as a composite mapping of individual planar regions that are about 40 mm in height and 50 mm in width (vertical configuration) and about 33 mm in height and 53 mm in width (horizontal configuration), i.e. field of view for the common overlap region of both cameras. Statistics were obtained from about 500 to 700 individual image pairs, which were acquired at a rate of approximately 3 Hz. Hence, the processed results are presented as a composite mapping of individual planar regions, as shown in Fig. 10. Each field of view represented about 9000 vectors (vertical configuration) and 9900 vectors

(horizontal configuration) for the seeded-only flow, and 4950 vectors for the spray-only case (horizontal configuration). The spatial resolution of the measurements depends directly upon the pixel interrogation area (i.e. 16 pixels × 16 pixels, with a pixel size/resolution of 6.7 μm), resulting field of view, total number of pixels, and laser light sheet thickness (i.e. 2–3 mm), and indirectly on the seeding density. Using only seed particles, the spatial resolution was approximately 600–700 μm in the plane of the laser sheet, and with only the spray droplets, the resolution was about 1.5 mm. For the latter, because of the lower droplet concentration and larger droplet sizes a final *IA* of 32 pixels × 32 pixels was used. An adaptive correlation routine was used to process the image maps with a final *IA* of 16 pixels × 16 pixels (flow with seed),

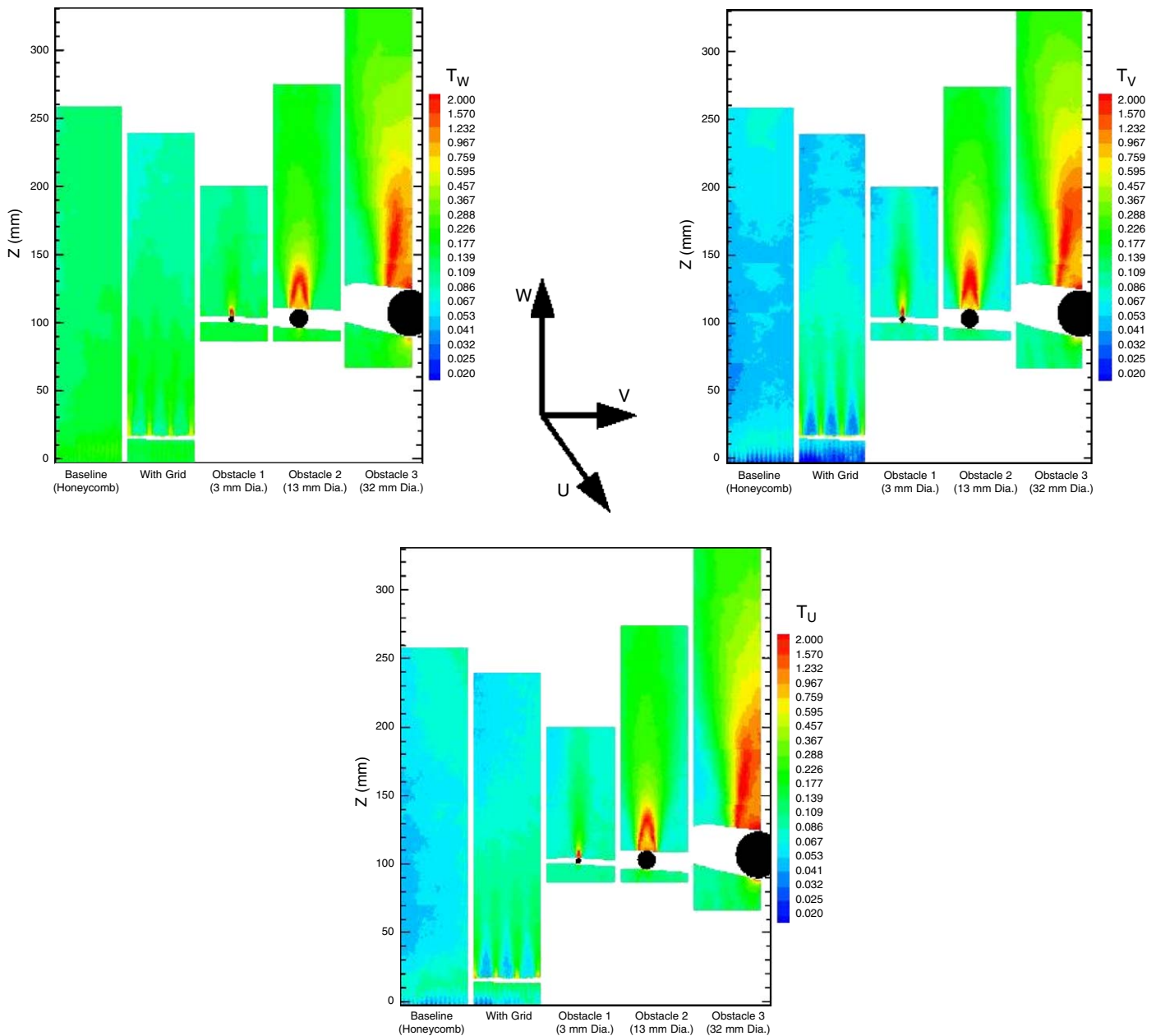


Fig. 12. Variation of mean streamwise ( $T_W$ ) and cross-stream ( $T_U$ ,  $T_V$ ) turbulence intensities with streamwise position ( $Z$ ).

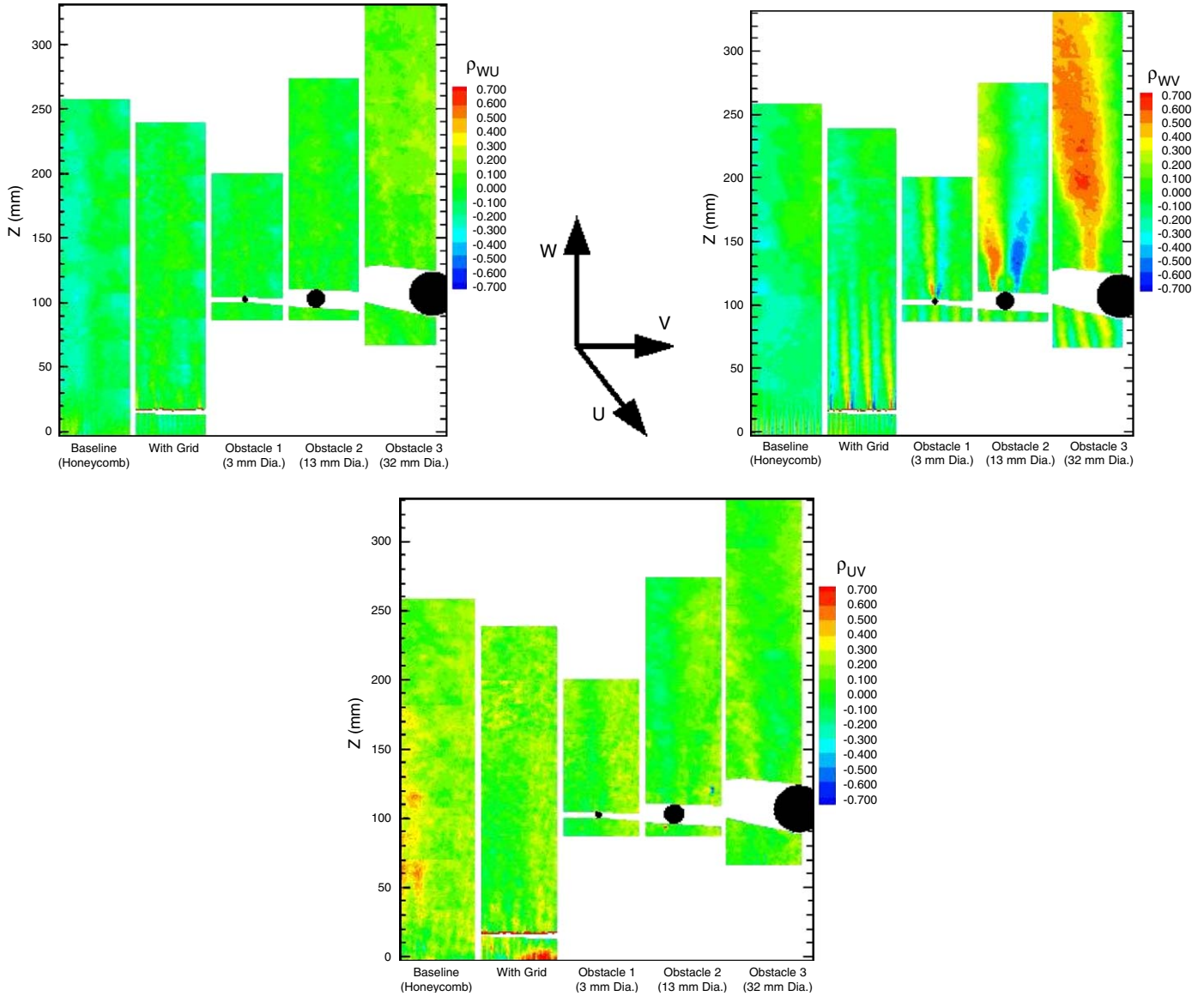


Fig. 13. Variation of turbulence correlation coefficients ( $\rho_{WU}$ ,  $\rho_{WV}$ ,  $\rho_{UV}$ ) with streamwise position ( $Z$ ).

while the initial  $IA$  was  $64 \text{ pixels} \times 64 \text{ pixels}$ . A 50% overlap was used to best take advantage of the image information. The velocity resolution was approximately  $5 \text{ mm/s}$  given the typical particle displacement within the interrogation area and additional sub-pixel refinement for correlation peak estimation (timing between frames was set to  $70 \mu\text{s}$ , resulting in particle displacements of about 20–25% of the typical  $32 \text{ pixel} \times 32 \text{ pixel}$  interrogation area). Calibration uncertainties for the three components of velocity,  $U$ ,  $V$ , and  $W$ , were estimated to be  $\varepsilon(W) = 0.1 \text{ mm/s}$ ,  $\varepsilon(V) = 0.1 \text{ mm/s}$ , and  $\varepsilon(U)/U = 4\%$ .<sup>3</sup> Note that  $W$  (streamwise) and  $V$  (cross-stream) are the components in the measurement plane, while  $U$  (spanwise across the cylinder) is the out-of-plane component, as determined from the stereoscopic PIV reconstruction.

<sup>3</sup>Uncertainties are at 95% confidence, unless otherwise stated.

A pencil fogger was used to generate water-based aerosol particles approximately  $1 \mu\text{m}$  in diameter. A separate supply of air (negligible with regard to the total air flow supplied for the experiment) was used to transport the aerosol from an enclosed aluminum box containing the fogger into the main air stream downstream of the distributor plate (see Fig. 1 for the vertical configuration and Fig. 3 for the horizontal configuration). A tube with several holes was stretched across the passage to enable dispersion of the aerosol across the measurement area. The PIV images were obtained in the plane illuminated by the laser light sheet, which was oriented normal to a cross section of the obstacle. The time between the images was determined by the time between laser pulses.

Measurements of the flow field were carried out along the cylinder centerline at the measurement areas shown in Fig. 10. After images were obtained for one measurement

area, the traverse was used to reposition the experiment at the next adjacent region (see Fig. 10), and in this way spatial profiles were obtained after joining the images. For the vertical configuration, PIV measurements were also carried out along two additional off-axis planes of  $\pm 25$  mm from the centerline location. Three cylinders of varying diameter were investigated with the vertical configuration. Three cases were recorded with the horizontal configuration using the largest diameter cylinder: (1) with seed only, (2) with droplets only, and (3) with both seed and droplets, in order to isolate the effects of both the droplets and particles on the flow field dynamics. These cases were repeated for both unheated and heated cylinder conditions. Measurements of the flow field were also carried out along the centerline of the BCC. Two additional off-axis planes were interrogated to map out one quadrant of the BCC: (1) between the center and two outer spheres, and (2) slightly outside of the center of the two outer spheres.

### 3. Results and discussion

#### 3.1. Vertical experimental configuration

Particle image velocimetry was used to obtain instantaneous two-dimensional images of the flow field velocity (i.e. three components of velocity). These images were then used to construct profiles of the streamwise ( $W$ ) and two cross-stream ( $U$ —spanwise along the cylinder length, and  $V$ —upward vertically from the cylinder) particle mean velocities (see Fig. 11), local mean turbulence intensity ( $T_i$ , where  $i = U, V, W$ , see Fig. 12), and velocity correlation

coefficients ( $\rho_{ij}$ , where  $ij = UV, UW, VW$ , and from which the Reynolds stresses can be derived, see Fig. 13), both upstream and downstream of the cylinder, and along the central plane of the honeycomb rectangular cross-sectional area.

The local mean turbulence intensity for each component is defined as

$$T_i = \frac{\sigma_i}{\sqrt{U^2 + V^2 + W^2}}, \quad (1)$$

where  $\sigma_i$  is the root mean square of the fluctuating components of velocity

$$\sigma_i = \left[ \frac{1}{N-1} \sum_{k=1}^N (u_{ik} - U_i)^2 \right]^{1/2}, \quad (2)$$

where  $N$  is the total number of velocity vectors, and  $U_i$  ( $= U, V, W$ ) is the mean of the components of the individual velocity vectors,  $u_i$  ( $= u, v, w$ ).

The velocity correlation coefficients are given by

$$\rho_{ij} = \frac{\text{Cov}\{U_i U_j\}}{\sigma_i \sigma_j} \quad (-1 \leq \rho_{ij} \leq +1), \quad (3)$$

where  $U_i U_j = UV, UW, VW$  and

$$\text{Cov}\{U_i U_j\} = \frac{1}{N-1} \sum_{k=1}^N (u_{ik} - U_i)(u_{jk} - U_j), \quad (4)$$

where  $u_j$  is the component of the individual velocity vectors corresponding to  $U_j$ .

Each figure consists of five spatial profiles with the baseline (honeycomb only) profile presented on the left side of the graph, followed by a profile with the grid mesh in

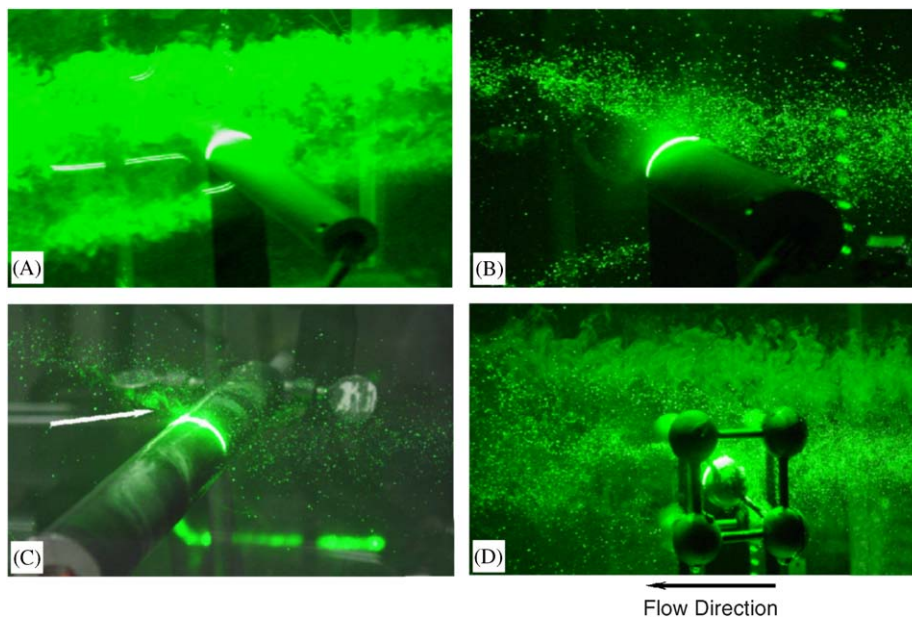


Fig. 14. Photographs of the (A) aerosol seeded flow field around the unheated cylinder, (B) droplet-laden flow field around the unheated cylinder, (C) droplet-laden flow field around the heated cylinder (arrow indicated presence of vapor layer), and (D) seed/droplet-laden flow field around the body-centered cube of spheres.

place, and then with the three cylinders. Downstream of the honeycomb (baseline profile), the flow field was found to be relatively uniform throughout the measurement field, as shown in Figs. 11 and 12 (maximum gas streamwise component of velocity,  $W \cong 4.5$  m/s, and maximum turbulence intensity,  $T_W \cong 13\%$ ), except immediately downstream of the honeycomb. The local jetting downstream of the honeycomb exit decays with increasing streamwise distance, and becomes negligible at about 25 mm. Based on this observation, the grid mesh that is used to generate turbulence was placed at this location.

The flow downstream of the grid mesh was obtained along the central plane of the measurement region. Due to the presence of the mesh, flow nonuniformities formed downstream of the mesh and relaxed to roughly a homogeneous state of 9% turbulence intensity in each direction at about 100 mm downstream of the honeycomb ( $W \cong 4.0$  m/s). The obstacles were placed at this location,

shown in Figs. 11–13 as black circles, to study the evolution of the turbulent flow around the cylinders in this environment. Fig. 11 indicated that the free stream air velocity reached about 5.0 m/s around the side of the cylinders, and the flow behind each cylinder formed a recirculation region ( $W \cong -1.0$  m/s). The reverse flow behind the cylinders appears to extend about two cylinder diameters downstream. The turbulence intensity increased behind the cylinders ( $T_W \cong 20\%$  in a banded region behind the obstacle). There was a significant correlation of the velocity fluctuations downstream of the cylinder between the streamwise and  $V$ -cross-stream components (an absolute value of 0.7 was reached for the correlation coefficient, see Fig. 13). This result is an indication of the shear between the free stream and recirculation region behind the cylinder. The flow was also found to decelerate to a stagnation region near the centerline of the upstream face of each cylinder. The overall flow characteristics around

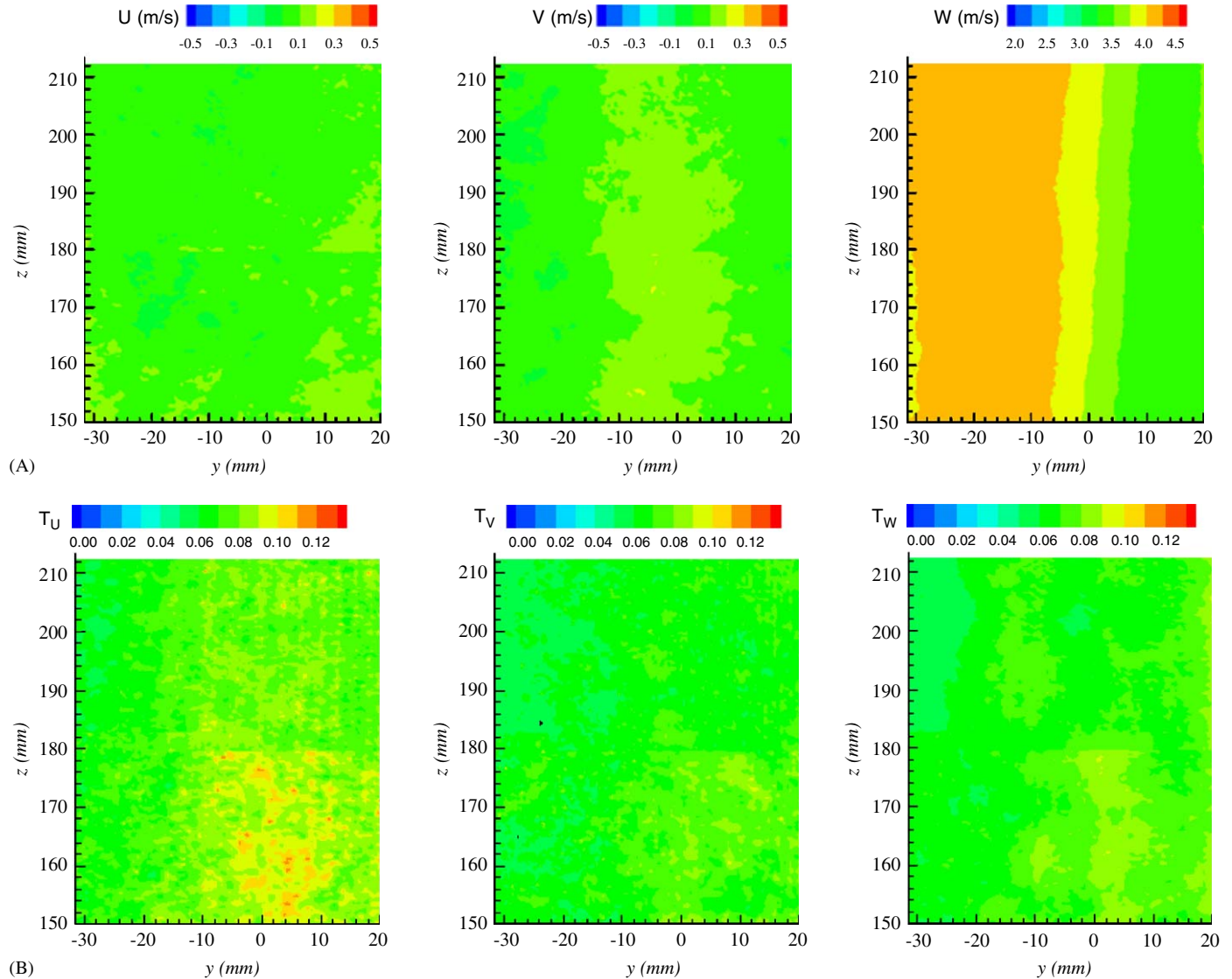


Fig. 15. Variation of the components of the (A) free stream mean velocity ( $U, V, W$ ), and (B) turbulence intensity ( $T_U, T_V, T_W$ ) with spatial position.

each cylinder appeared to be similar, except that the features grew proportional to the cylinder diameter.

### 3.2. Horizontal experimental configuration

#### 3.2.1. Flow visualization

The droplet-laden flow field was recorded with a high-resolution digital camera, which provided both still images and movies at 9 frames/s, and the planar laser light from the PIV system. Examples of the observed droplet/particle transport processes are shown in Fig. 14 for (A) aerosol seeded only and (B) droplet only flow over the unheated cylinder, (C) droplet-laden flow over the heated cylinder, and (D) combined droplet and seeded flow over the BCC. For the seed only case, entrainment into the turbulent flow field (see Fig. 14A) resulted in a relatively high concentration of particles observed in the cylinder wake, similar to the findings of Wang et al. [38]. On the other hand, for the spray only case (see Fig. 14B), droplets in the center of the spray impinged on the cylinder surface, while those droplets at larger radial positions were transported around and past the cylinder. Few larger size water droplets (as defined by the relative light intensity noted in the images) were observed in the cylinder's wake, but this region was abundant with smaller size droplets. There was no visual evidence of secondary breakup of the droplets (i.e. splashing) [29]. It was observed that water droplets dripped off the cylinder (not evident from Fig. 14B) at a rate of approximately 6.5 mL/min for the unheated cylinder. Using digital high-speed photography, impinging droplets were also observed to rebound off the surface back into the free stream. When the cylinder was heated to 423 K, there was significant cooling of the upstream face of the cylinder to about 351 K. The droplet-laden flow over the cylinder appeared to be qualitatively similar to the unheated case except along the shear layer downstream of the cylinder. In this region, a vapor layer formed (see arrow in Fig. 14C), which was presumed to be the result of vaporization of the liquid that wetted the hot surface. Dripping of water droplets was not observed for the heated cylinder presumably due to droplet vaporization.

The transport of droplets through the BCC (see Fig. 14D) was interesting in that both the spheres and connecting rods (that act like cylinders) impede droplet transport, while the flow field traversing through the obstacle (i.e. between the spheres and rods) provided a relatively unobstructed path for the entrained droplets (recall that the nominal blockage ratio was about 64%). Dripping was observed from each sphere at a rate of approximately 1 droplet/s. If one assumes that droplets fall off each sphere at this rate, one can determine that this liquid represents approximately 4.5% of the inlet water flow (assuming a dripped droplet diameter of 8.5 mm, which was an estimated largest droplet size observed from digital movies). Although the BCC had more dripping of liquid than the cylinder, the majority of the spray was still able to traverse the obstacle.

#### 3.2.2. Free stream conditions

Particle image velocimetry was used to obtain the three components of velocity for both the atomizer-generated droplets and fogger-generated aerosol particles. The spatial profiles were reconstructed using the same coordinate system as for the vertical configuration, but now referenced by the position of the grid mesh and atomizer face. Little difference was found in the characteristics of the homogeneous turbulent flow field, although the orientation of the plastic chamber was changed and an atomizer was incorporated into this configuration.

Characterization of the flow field without the obstacle offered a baseline condition, which was important for comparison of experimental results, or input/validation of any modeling effort. Hence, measurements were carried out at planar locations *A* and *B* (see Fig. 10). Results for the air mean velocities and corresponding turbulence intensities are shown in Fig. 15. The flow was essentially unidirectional (i.e. in the streamwise direction,  $W$ ), with a uniform streamwise velocity upstream of the cylinder. The PIV results indicated that the 'nominal' streamwise velocity,  $W_0$ , was approximately  $3.8 \pm 0.3$  m/s, which

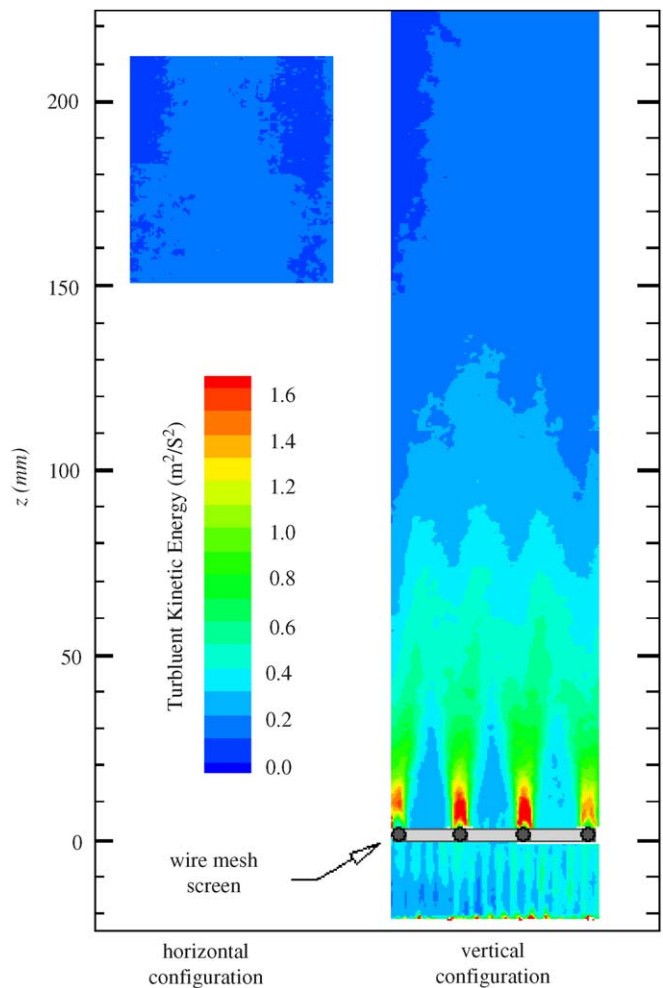


Fig. 16. Comparison of the free stream total turbulence kinetic energy from the vertical and horizontal configurations.

corresponds to a Reynolds number of about 3134 (based on the grid cell size and an air kinematic viscosity of  $0.154\text{cm}^2\text{s}^{-1}$ ), still in the turbulence regime for grid-generated turbulence [39]. The ‘nominal’ velocity is defined as the free stream mean air velocity obtained over the full measurement domain. The local mean turbulence intensity for each component was 7.8%, 6.7% and 7.0% across the flow field for  $U$ ,  $V$  and  $W$ , respectively. The variation between each component was small and for all practical purposes, the assumption of homogeneous turbulence was a valid one. To further characterize the turbulent flow at the location where the cylinder was to be placed, the free stream total turbulence kinetic energy for the horizontal and vertical configurations is shown in Fig. 16. The figure presents  $k_t$ , given as

$$k_t = \frac{1}{2}(\sigma_U^2 + \sigma_V^2 + \sigma_W^2) \quad (5)$$

and indicates the development of turbulence downstream of the grid mesh. These measurements were somewhat smaller than the values obtained for the vertical config-

uration because the cylinder was placed further downstream at approximately  $Z = 185\text{mm}$  (as opposed to  $Z = 75\text{mm}$  for the vertical configuration).

### 3.2.3. Air flow field

Since the spray influences the flow around the cylinder, it was necessary to examine under droplet-laden conditions the state of the airflow by trying to isolate the aerosol seed velocity. Results from the stereoscopic PIV measurements are presented in Figs. 17 and 18, for the unheated and heated cylinder, respectively. The figures include air mean and root mean square velocities, all normalized by the nominal streamwise velocity of  $W_0 = 3.8\text{m/s}$ .

The information presented in the figures is velocity determined under droplet-laden flow conditions, and with the airflow seeded with aerosol particles. The sparseness of the droplets, as well as their larger relative image size, created the opportunity to determine the velocity of the seeded airflow, mostly unbiased by the presence of the droplets. While ideally it would be desirable to optically

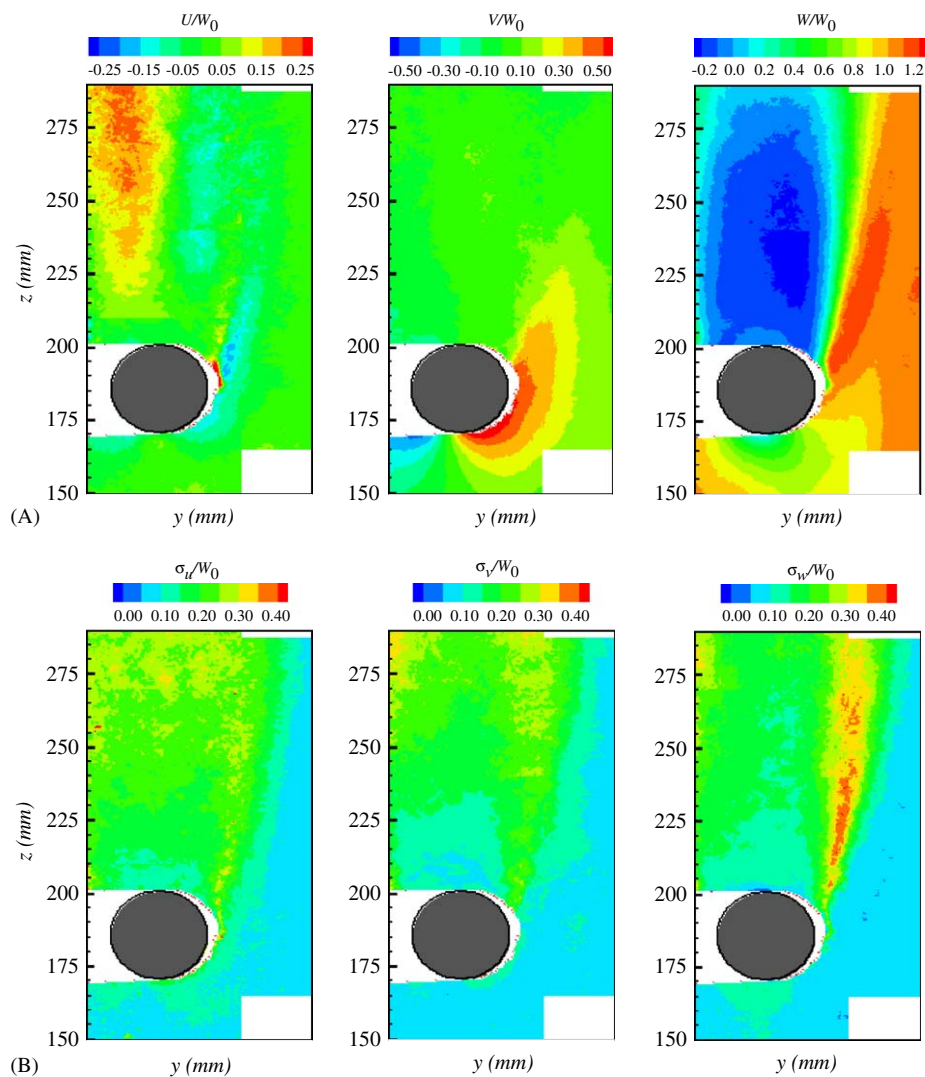


Fig. 17. Variation of the normalized air (A) mean velocity ( $U/W_0$ ,  $V/W_0$ ,  $W/W_0$ ) and (B) root mean square velocity ( $\sigma_U/W_0$ ,  $\sigma_V/W_0$ ,  $\sigma_W/W_0$ ) with spatial position for droplet-laden flow around the unheated cylinder (note that contour levels are different for the mean velocities).

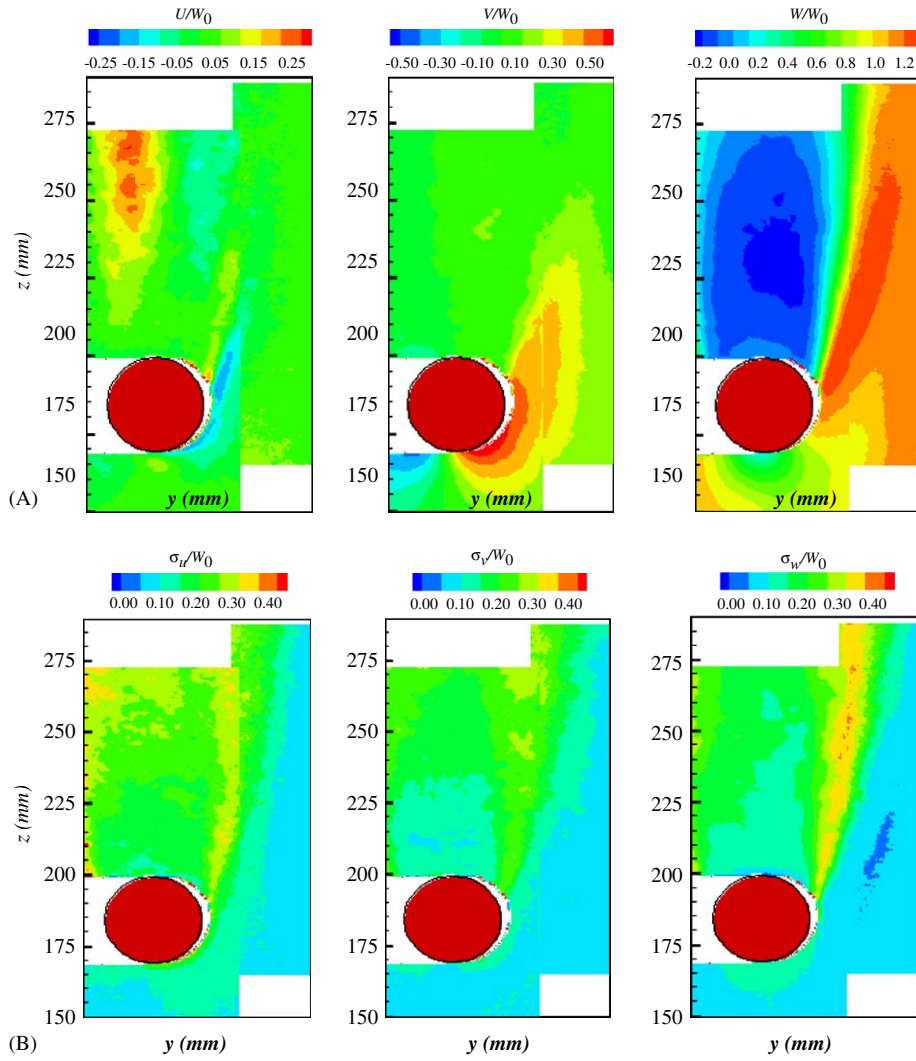


Fig. 18. Variation of the normalized air (A) mean velocity ( $U/W_0$ ,  $V/W_0$ ,  $W/W_0$ ) and (B) root mean square velocity ( $\sigma_u/W_0$ ,  $\sigma_v/W_0$ ,  $\sigma_w/W_0$ ) with spatial position for droplet-laden flow around the heated cylinder (note that contour levels are different for the mean velocities).

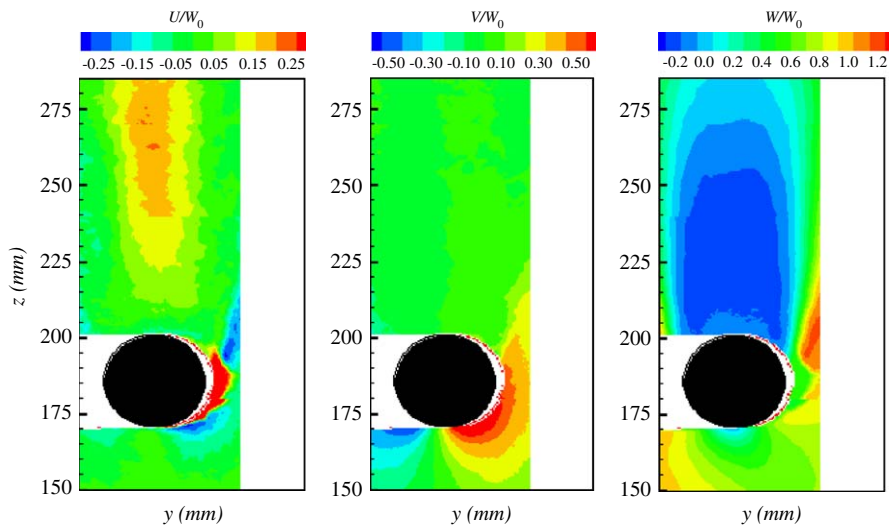


Fig. 19. Variation of the normalized air mean velocity components ( $U/W_0$ ,  $V/W_0$ ,  $W/W_0$ ) with spatial position for the seeded flow only (in the absence of the spray) around the unheated cylinder.

de-couple the two image signals, and thus obtain independent velocity estimates for the aerosol particles (air flow) and spray droplets, and thus the local droplet/air relative velocity, dealing with the difficulty of implementing an optical discrimination methodology was outside of the scope of this study.

With the seeding density typically much higher than the droplet density, especially in the wake region, a final interrogation area of 16 pixels  $\times$  16 pixels was used to determine the correlation function between interrogation areas in each image pair. While the PIV correlation technique estimates the average displacement of particles within an interrogation area, the validity of the estimate is a strong function of the number of particles that correlate well within the interrogation area (as shown in Ref. [40]). The smallest possible interrogation area that still detected

the signal of the aerosol particles was chosen to reduce the bias towards larger droplets. It was assumed that one or two larger droplets would not bias strongly the signal from 20 to 30 smaller aerosol droplets. Also, a 12-bit camera was used with better intensity resolution to enhance the cross-correlation signal-to-noise ratio. Therefore, since the number count of the aerosol particles was always higher than that of the spray droplets (as a result of the aperture effect of the chosen smaller interrogation area), the displacement estimate was biased in favor of the seeded flow.

It was not possible to examine absolutely the above reasoning in the present flow, since the spray influences the airflow around the cylinder. Even so, measurements of the seeded flow without the spray were also obtained, and results of the mean velocity components are presented in

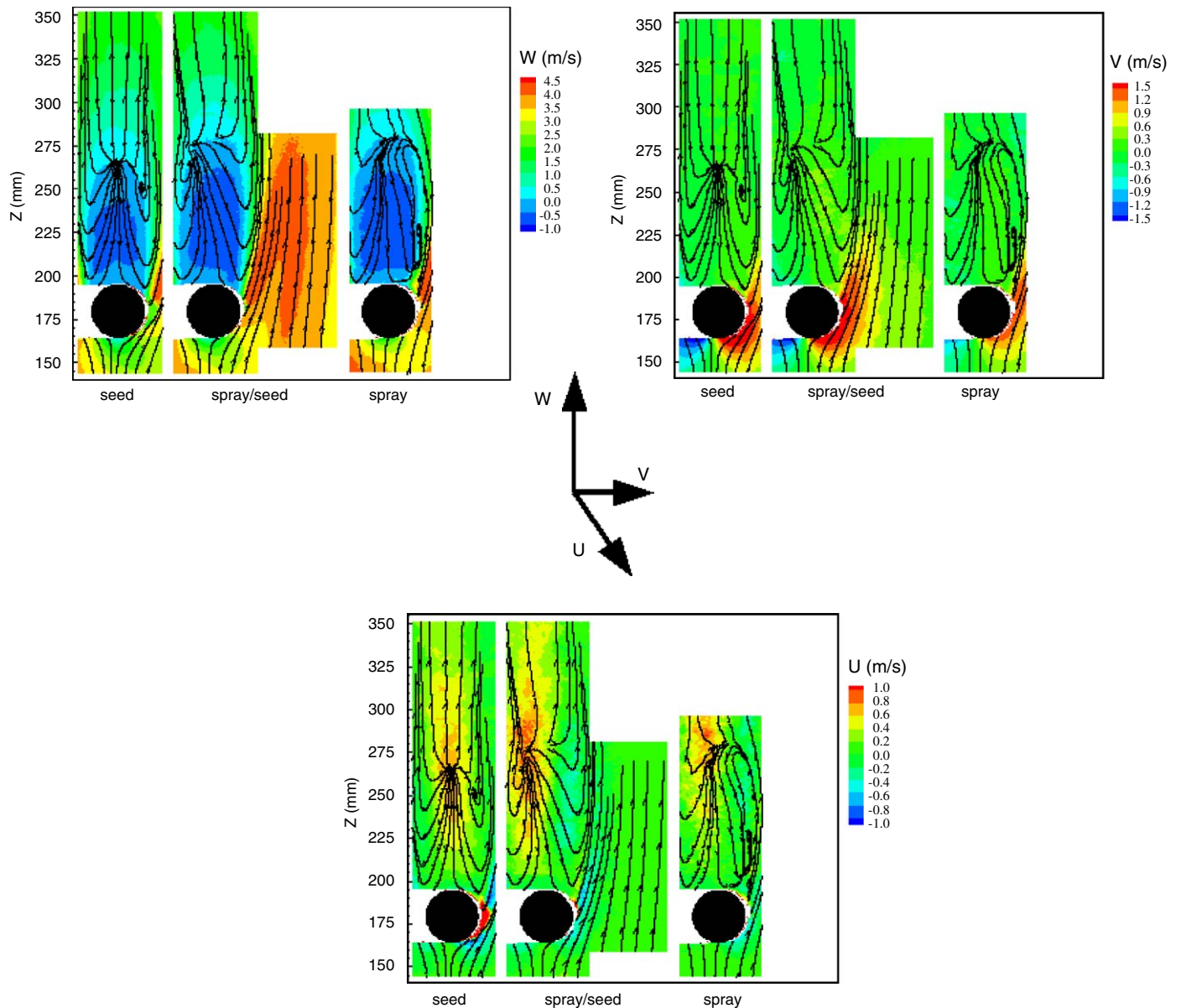


Fig. 20. Variation of the droplet mean streamwise ( $W$ ) and cross-stream ( $U$ ,  $V$ ) velocities with streamwise position ( $Z$ ) for the unheated cylinder. Contours are the stream traces of the in-plane vectors obtained from the streamwise and  $V$ -cross-stream components of velocity.

Fig. 19. Comparison with similar results obtained for the droplet-laden flow over the unheated cylinder (see Fig. 17) indicates that the spray influences the flow, as expected. The influence is modest, especially upstream of the cylinder for the  $U$ - and  $V$ -components of velocity. The latter component compares well in both cases (i.e. seeded airflow only and droplet-laden seeded airflow), providing some level of confidence in the post-processing approach used to determine the airflow velocity for images containing both seed and droplets. As will be discussed for the velocity of the spray only case, the  $V$ -component of velocity immediately upstream of the cylinder was significantly smaller than that for the seed only case, owing to the high streamwise momentum of the droplets along the spray centerline.

Comparison of the airflow velocity fields presented in Figs. 17 and 18 indicates that the air velocity reached a maximum streamwise value as the flow accelerated around the cylinder, which is 15–20% higher than the nominal streamwise value. The shear layer that forms past the cylinder is quite evident in the streamwise root mean square velocity figures, for both the unheated and heated cylinder cases. Although, the velocity in the shear layer indicates little magnitude difference between the two cases, the mean streamwise velocity maps show evidence that for the heated cylinder case the shear layer stretches further downstream past the cylinder. The  $V$ -component of the air velocity increases significantly around the side of the cylinder, reaching a value of approximately 50% of the nominal streamwise velocity. In the shear layer region,

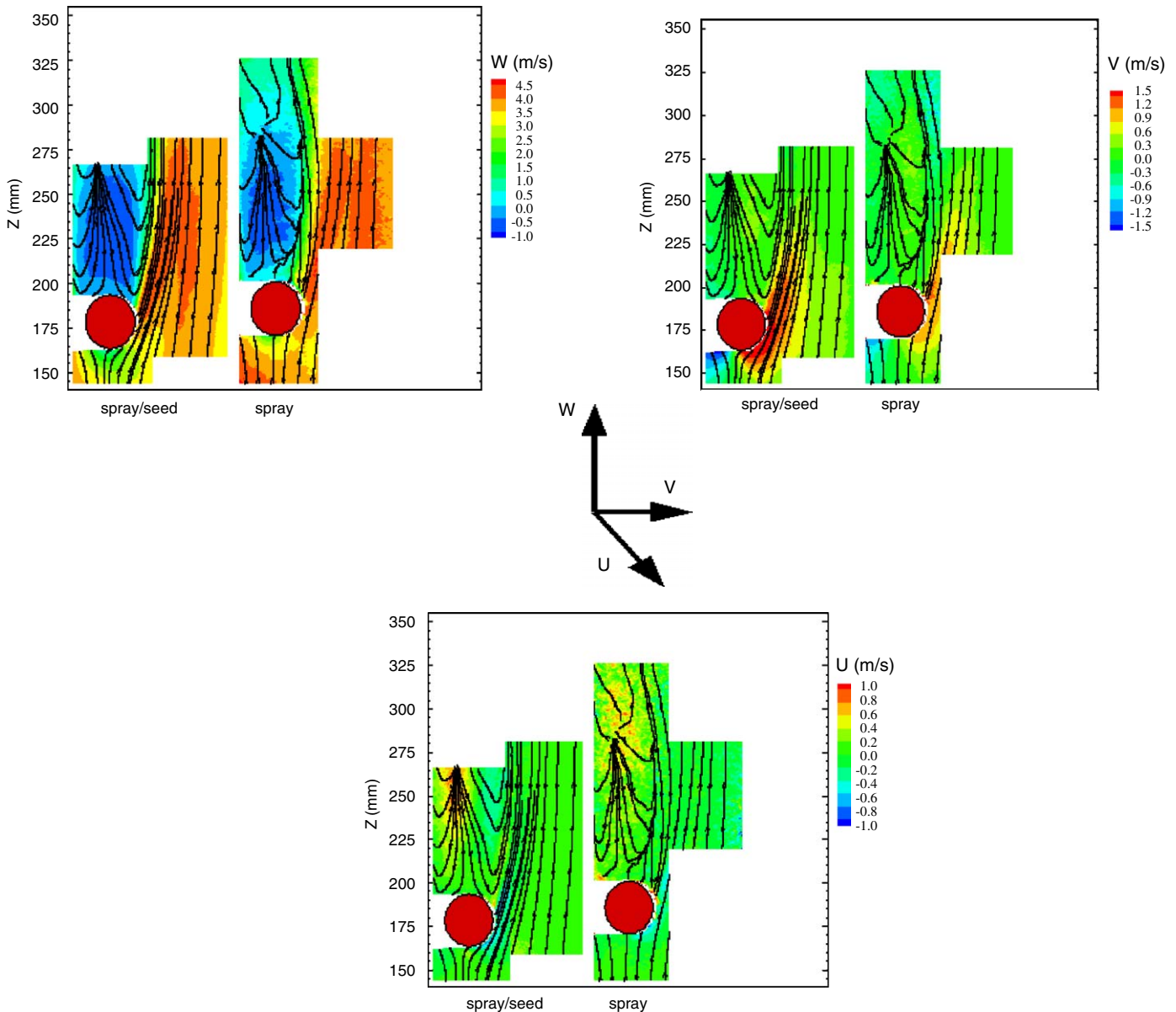


Fig. 21. Variation of the droplet mean streamwise ( $W$ ) and cross-stream ( $U$ ,  $V$ ) velocities with streamwise position ( $Z$ ) for the heated cylinder. Contours are the stream traces of the in-plane vectors obtained from the streamwise and  $V$ -cross-stream components of velocity.

the difference between the unheated and heated cases is that the heated cylinder has a slightly higher cross-stream velocity over a longer distance downstream of the cylinder. On the other hand, a magnitude difference of the values of  $\sigma_W$  in the shear layer is noted between the two cases. This turbulence is lower for the heated case, especially immediately downstream of the cylinder. Lower values of  $\sigma_W$  indicate less diffusion, which would support the apparent longer shear length observed for the heated case. A recirculation zone also develops behind the cylinder, with reverse velocities reaching about 20% of the nominal streamwise velocity. The reverse flow appears to extend about two cylinder diameters downstream, and no significant length difference is apparent between the two cylinder scenarios (i.e. unheated and heated).

3.2.4. Spray characteristics—droplet velocity

Comparison of the velocity fields obtained with water droplets and aerosol seed indicated that dispersion of

droplets/seed around the obstacle is dependent on the droplet/seed size. A more detailed analysis of the dependence of size on transport of droplets around the cylinder is given in Ref. [29]. For example, the three components of droplet velocity for the droplet-laden flow over the unheated cylinder are presented in Fig. 20. In this figure, three cases are presented that represent the flow with the seed only, both seed and spray, and spray only. The black circle represents the position and size of the cylinder. The black contours lines represent stream traces (i.e. direction) of the in-plane  $V$ – $W$  velocity vectors. (Note the change of contour color scale in Fig. 20 and subsequent figures.) The seed only case compares with the results from the vertical configuration (see Fig. 11), and was discussed in detail earlier. Comparison of the two cases with spray to the seed-only case indicates that the recirculation zone is somewhat larger for the spray cases. Larger size droplets require a longer transit time to interact with the turbulent flow field and reduce their initially higher momentum to be entrained into the recirculation zone, if at all.

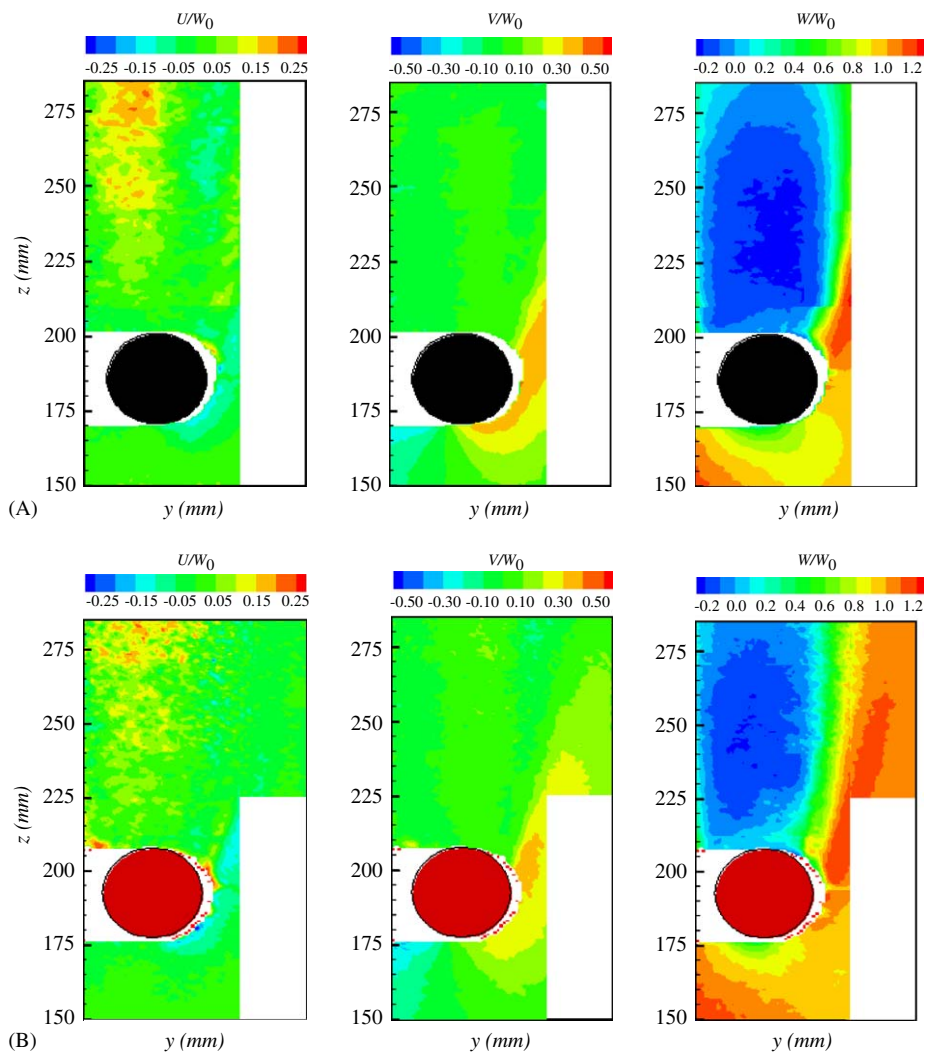


Fig. 22. Variation of the droplet normalized mean velocity components ( $U/W_0$ ,  $V/W_0$ ,  $W/W_0$ ) with spatial position around the (A) unheated and (B) heated cylinders.

The stream trace (contour lines) also shows an unexpected pattern behind the cylinder near the stagnation point. Instead of presenting closed loops that indicate a recirculating pattern, the contours appear to emanate from the stagnation region. One possible explanation is that in the stagnation region the  $U$ -component of velocity reaches an absolute value of nearly 0.8 m/s, indicating a strong spanwise flow along the length of the cylinder in both directions. Spanwise flow is also found along the upstream side of the cylinder. It appears to be generated by the cylinder and may be related to the finite cylinder length (with an aspect ratio of about 10:1) [41].

The droplet-laden flow over the heated cylinder, presented in Fig. 21, is similar to the unheated cases (only the spray and combined spray/seed cases are presented in the figure since the seed only case was not expected to change from that of the unheated cylinder). When the heated cylinder is compared to the unheated cylinder the following differences are found for the spray-only case: (1) a stronger streamwise flow and weaker reverse flow behind the cylinder (see  $W$ -component of velocity), (2) a weaker radial flow around the side of the cylinder (see  $V$ -component of velocity), and (3) the  $U$ -component cross-stream flow extends further downstream of the cylinder. These results are consistent with that of a heated flow field, in which the reduction in gas density (and concomitant reduction on droplet drag) results in increased streamwise droplet-laden flow around the cylinder.

Normalized mean velocity contours with only the spray droplets (in the absence of aerosol seed), are shown in Fig. 22 for both the unheated and heated cylinders. In light of the droplet sparseness during each image pair acquisition, especially in the wake region, a moving ensemble averaging technique was implemented, whereby several image pairs were initially averaged (separately for Images A and B) to produce a composite image pair prior to implementing the PIV cross-correlation methodology. The ensemble size chosen was three, and thus  $N-2$  composite image pairs were created for each planar acquisition. Consequently, the vector maps determined from each composite image pair were used for further analysis.

Comparison of the normalized mean values for the unheated cylinder indicates that the spray droplets entrain into the wake region, with their  $U$ - and  $W$ -components of velocity comparable to the air flow velocity (shown in Fig. 17). A difference is, however, noted for the  $V$ -component of velocity near and around the surface of the cylinder. While the air stream velocities indicate strong flow redirection due to the presence of the obstacle, the droplet velocities in the same region are 40–50% less than the air cross-stream velocity at the same location. This indicates that the droplets fail to follow the flow around the cylinder due to their larger streamwise momentum, leading to collisions with the cylinder for droplets within the core region of the spray. The core spray region is defined by estimating which droplets are destined to impact directly with the cylinder, based on the velocity field upstream of

the cylinder, as shown in Fig. 23. The figure presents color-coded streamlines, coded by the normalized magnitude of the total velocity, for the case of droplet-laden airflow over the unheated cylinder. In addition to these color-coded streamlines, a solid white line estimates the division streamline between the flow transported around the

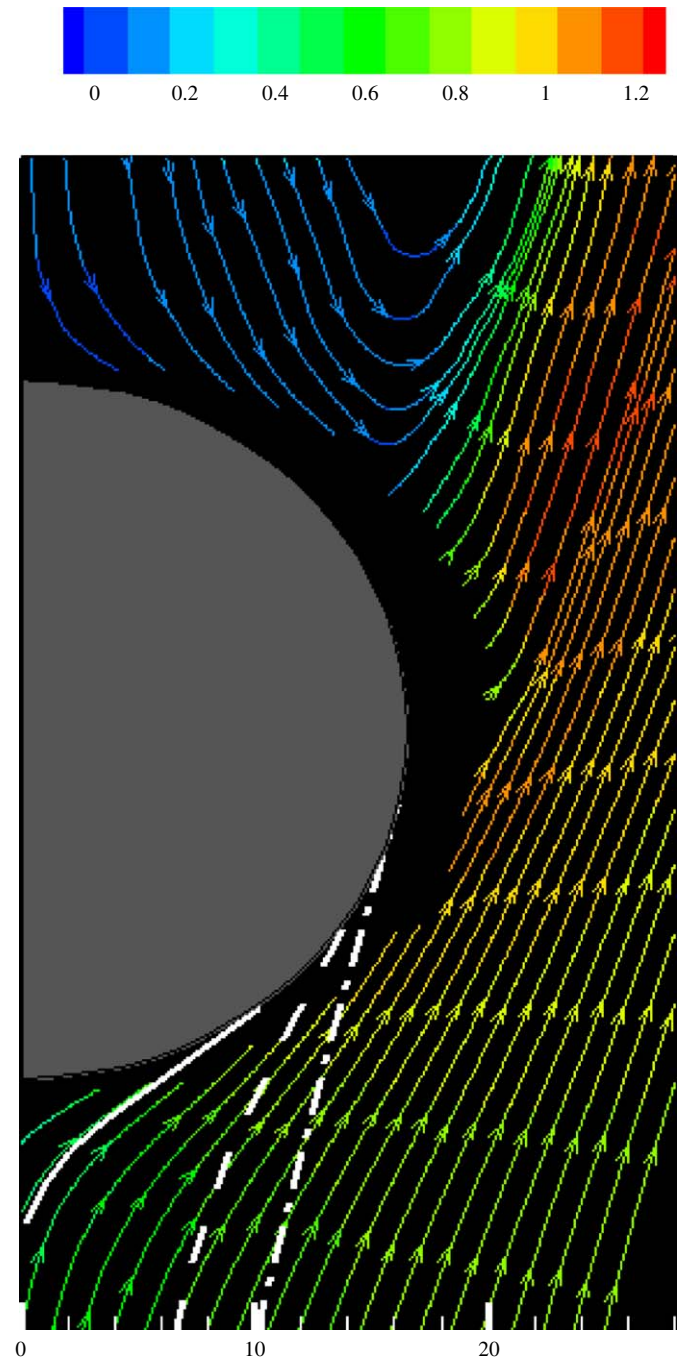


Fig. 23. Color-coded streamlines for droplet-laden air flow past the unheated cylinder (normalized to the magnitude of the total velocity); white lines indicate the dividing streamlines separating the flow that impacts the cylinder to that transported around it: *solid*—droplet-laden air flow with the unheated cylinder; *dash*—droplets with the unheated cylinder; and *dash-dot*—droplets with the heated cylinder (dimensions are in mm).

cylinder (on the right of the line) and the flow impacting with the cylinder (on the left). The solid line is the estimate for the droplet-laden flow around the unheated cylinder (i.e. droplets and seed). In a similar fashion, the dashed white line was constructed for the spray flow past the unheated cylinder, based on the planar velocity components that exist upstream of the cylinder. Note that the contribution of the entrained seed in the droplet-laden airflow case results in the solid white streamline positioned closer to the center of the flow than in the droplet only case (dashed line). This result further supports the methodology used to separate airflow velocity from droplet velocity in the droplet-laden flow cases, as described earlier.

The results for the spray flow around the heated cylinder are similar to that of the unheated cylinder (see Fig. 22). However, the  $V$ - and  $W$ -components of velocity are noticeably smaller. An estimate on the dividing streamline is also shown in Fig. 23, by the white dash-dot line. The reduced magnitude of the cross-stream velocity components results in an increase in the width of the spray core

region. Thus, the results indicate greater droplet impingement on the cylinder surface than for the unheated cylinder, and less droplet entrainment into the shear layer. In the wake region, there is less droplet entrainment into the recirculation region for the heated cylinder, as compared to the unheated cylinder. Also, the surface temperature along the downstream side of the cylinder is presumed to be higher than on the upstream side, since it is not quenched by droplet impingement and wetting of the surface, and may contribute to the diminished presence of droplets in this region.

The root mean square velocities for the ambient seeded case ambient spray/seed case, and heated spray/seed case (assuming the heated seed only case is similar to the corresponding ambient case) are presented in Fig. 24. The root mean square velocity increases behind the cylinder, reaching a maximum value of about 1.4 m/s in the shear layer region for  $\sigma_W$  and  $\sigma_V$  of the heated cylinder case. There appears to be little difference when the contribution of the spray is considered, however, for the heated cylinder

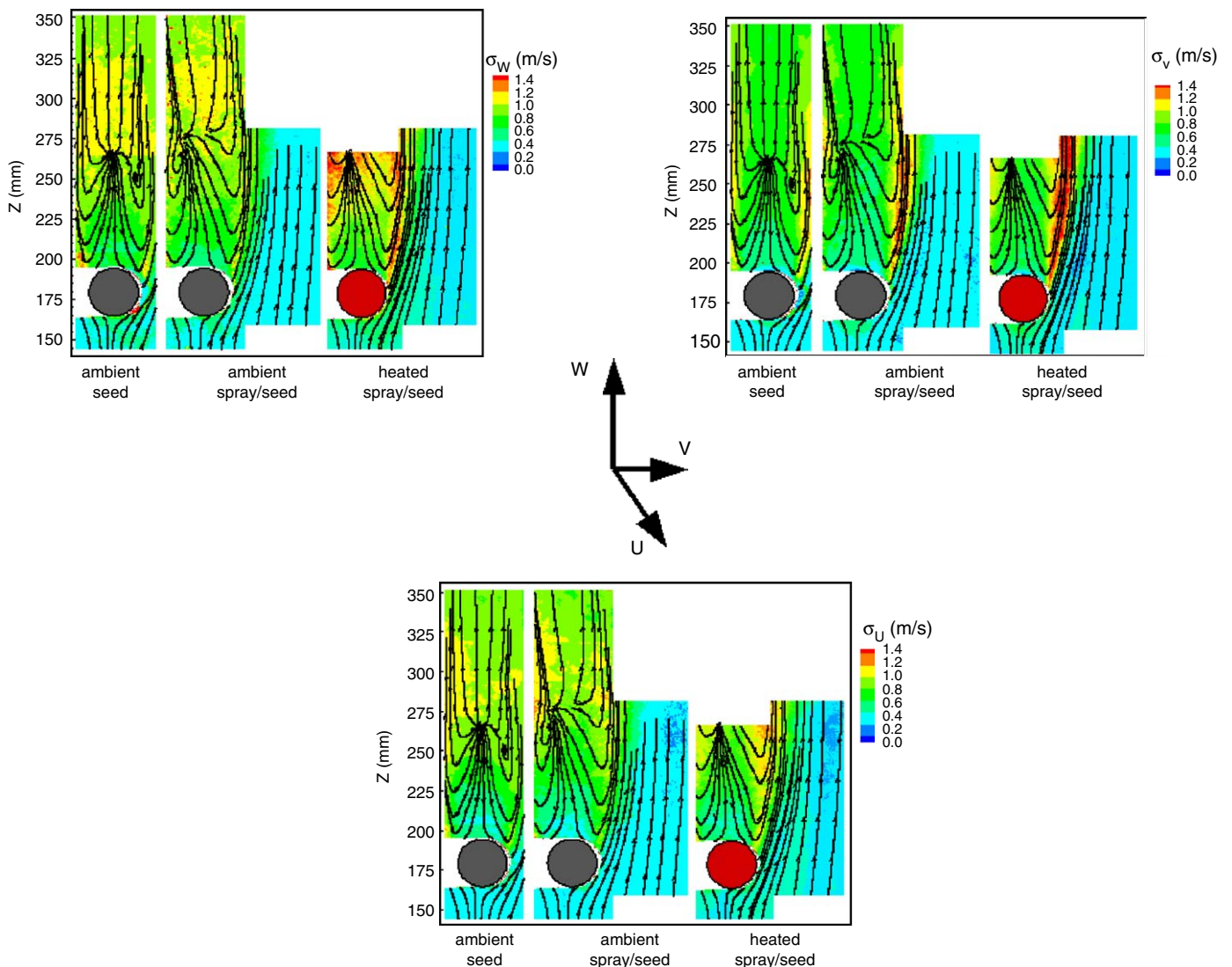


Fig. 24. Variation of the root mean square velocity ( $\sigma_U$ ,  $\sigma_V$ ,  $\sigma_W$ ) with streamwise position ( $Z$ ).

case, the root mean square velocity is significantly higher along the shear layer region than for the unheated cylinder case.

There is a significant correlation of the velocity fluctuations downstream of the cylinder between the streamwise and  $V$ -cross-stream components, as indicated in Fig. 25 for the seed only case. An absolute value of 0.7 is reached for the correlation coefficient, similar to the results given in Fig. 13. This result is indicative of the shear between the free stream and reverse flow region downstream of the

cylinder (i.e. the fluid flow stagnation point is off the downstream face of the cylinder). The presence of the spray appears to have negligible effect on the results when comparing the seed only and spray/seed cases in Fig. 25. The flow also decelerates near the stagnation region along the centerline at the upstream face of the cylinder.

Fig. 26 presents the velocity field around the BCC for the combined spray/seed case. Although the configuration is more complicated, there are still similar features to the cylinder case. The flow accelerates around the spheres and

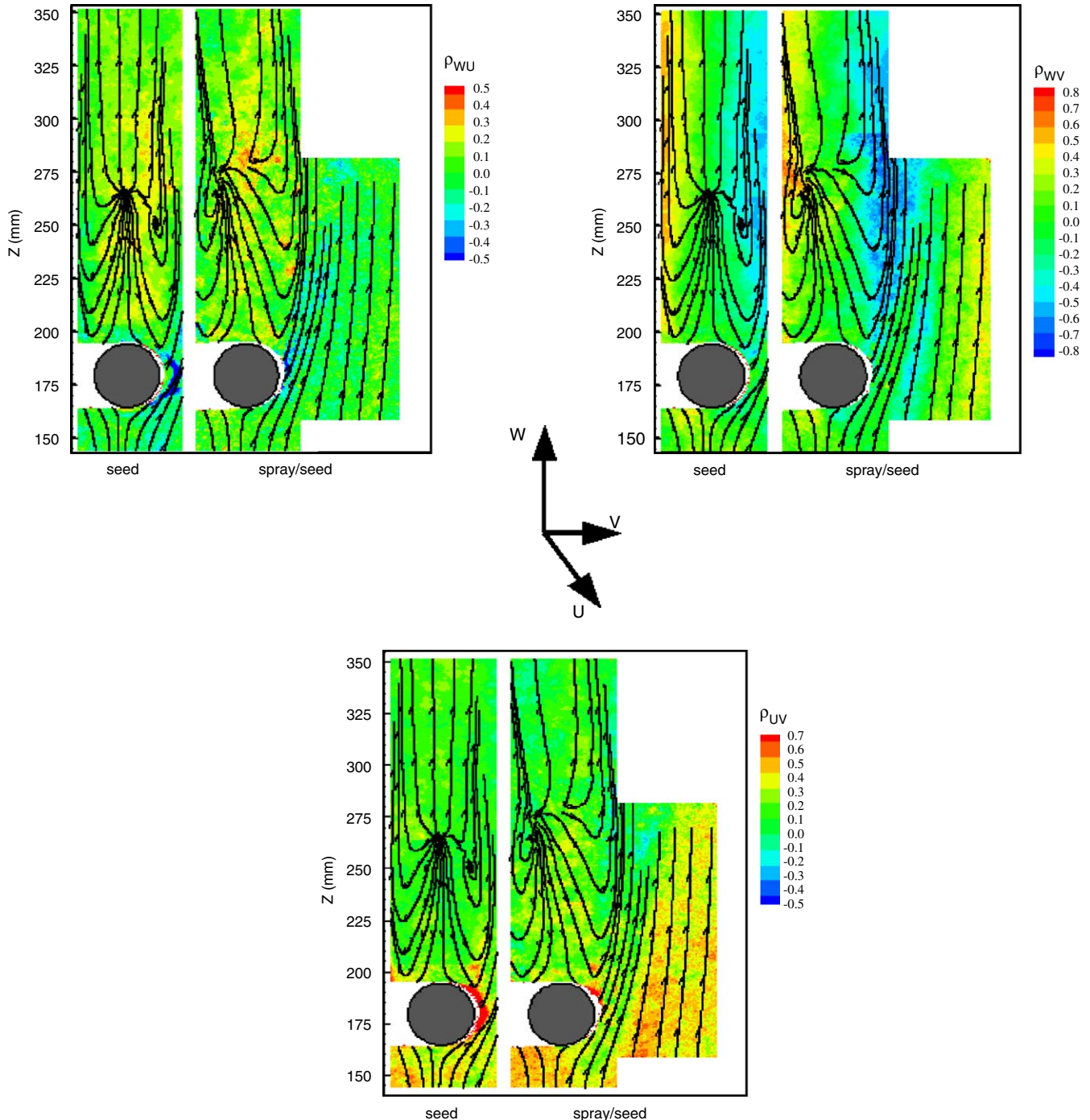


Fig. 25. Variation of the turbulence correlation coefficients ( $\rho_{WU}$ ,  $\rho_{WV}$ ,  $\rho_{UV}$ ) with spatial position (Z).

there is reverse flow in the wake region. In addition, the presence of a cross-stream component of the flow is evident around the spheres. This cross flow may be a result of the three-dimensional nature of the spheres and flow field, and the transport of entrained droplets and aerosol particles through convoluted pathways of this obstacle.

3.2.5. Spray characteristics—droplet size

A semi-quantitative estimate for the relative droplet size of the spray can be obtained by considering certain characteristics of the PIV cross-correlation function. As mentioned earlier, each image pair is broken up into smaller image areas, called ‘interrogation areas’. For each

one of these interrogation areas a cross-correlation function is generated according to the PIV methodology. This cross-correlation function is a surface function, as presented in Fig. 8, that is characterized by its peak height and its peak half-width (i.e. width of the function at half its peak height value). While the location of the peak within the interrogation area is mostly independent of particle image size and appearance, the contrary is true about the width of the correlation function. The broadness of the correlation function has a strong dependence on how particles image onto the CCD, with larger apparent particles contributing to a broader correlation function, or larger peak half-width values. Thus, the cross-correlation

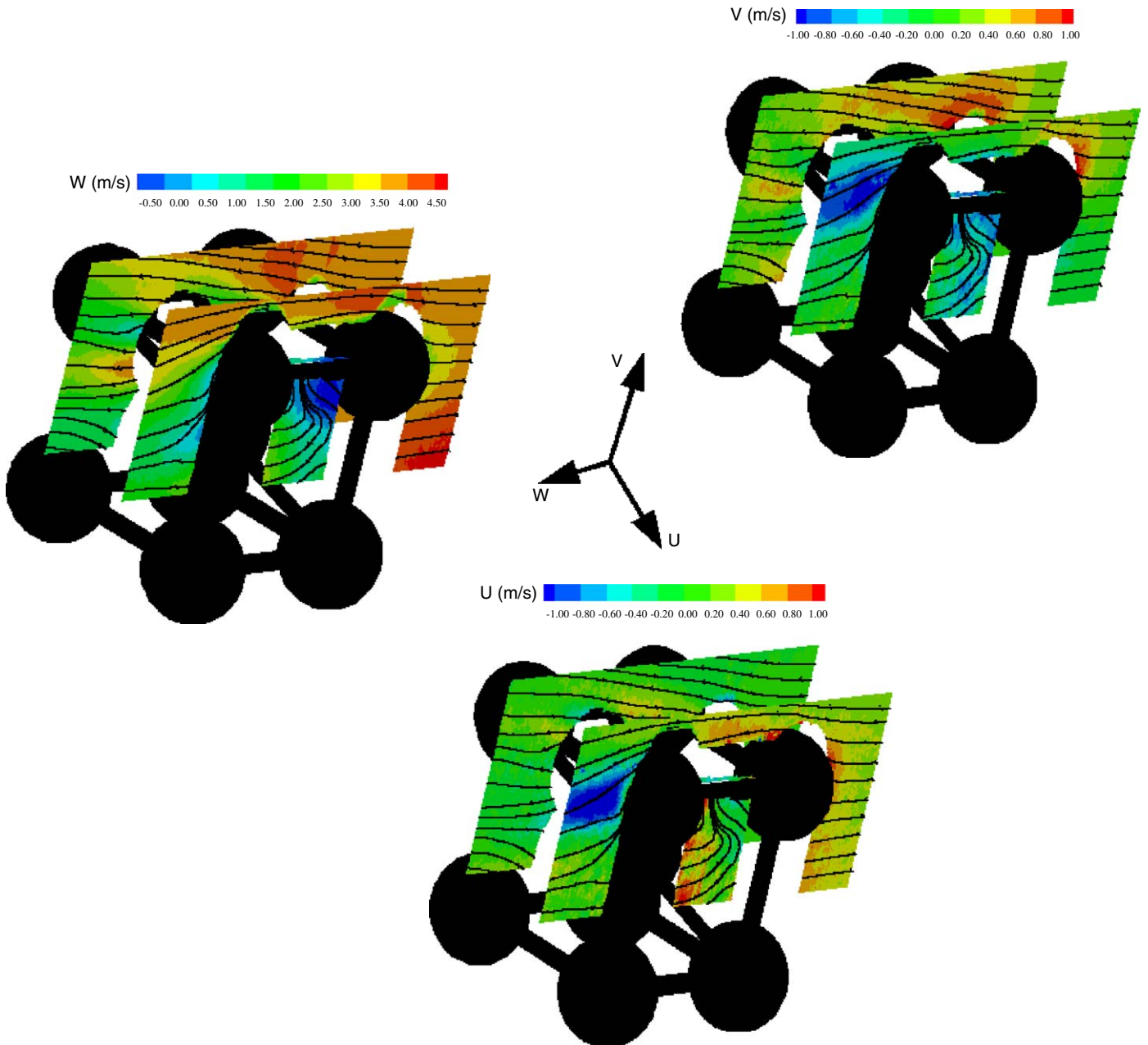


Fig. 26. Variation of the mean streamwise ( $W$ ) and cross-stream ( $U$ ,  $V$ ) velocities with streamwise position ( $Z$ ) for the body-centered cube of spheres. Contours are the stream traces of the in-plane vectors obtained from the axial and radial components of velocity.

peak half-width provides a semi-quantitative estimate for an “average” relative size of the ensemble of spray droplets within the interrogation area.

With the benefit of having one of the cameras looking at the flow nearly perpendicular to the illumination plane, an average correlation function field was generated from image pairs captured by this camera, providing nearly distortion-free imaging of the droplets. An average correlation field was generated using the methodology proposed by Meinhart et al. [42], whereby the correlation functions of many image pairs were first averaged prior to determining correlation peak characteristics. In such a way, the signal-to-noise ratio of the correlation function is dramatically improved, which is important in the present case, where regions exist that are sparsely populated by droplets, especially in the wake. The extracted information from three averaged ensembles of more than 150 correlation averaged image pairs is presented in Fig. 27. Shown is the relative cross-correlation peak half-width, normalized by the value upstream of the cylinder (i.e. at  $Z = 140$  mm and along the cylinder centerline), for the unheated and heated cylinder scenarios.

Upstream of the cylinder, the relative droplet pseudo-size indicates a 10–15% increase at off-axis locations in relation to the spray center, which is attributed to the hollow-cone nozzle design. Downstream of the cylinder, the presence of larger droplets in the shear layer is indicated by an increase in the relative peak half-width value, approximately 80–120% larger than in the spray core upstream of the unheated cylinder, while it is more than 200% larger for the heated cylinder. Note that the larger value obtained for the heated cylinder is to a large extent biased by the vapor formed due to droplet evaporation, which tends to broaden the correlation function due to the vapor’s flat intensity distribution. Hence, the semi-quantitative results of the current meth-

odology are not expected to capture the correct trend with regards to droplet size in the shear layer when comparing the unheated and heated cylinder cases.

In the wake region of the unheated cylinder, the estimate of the relative pseudo-size indicates the presence of droplet sizes smaller than those detected in the spray upstream of the cylinder. Determination of the size distribution in the recirculation region becomes difficult at positions near the aft cylinder surface. For the heated cylinder case, however, the relative pseudo-size estimate indicates that larger droplets are detected in the recirculation region than for the unheated cylinder. Again, these results for the heated cylinder may contain bias due to vapor being entrained into the wake region.

#### 4. Conclusions

Particle image velocimetry measurements were carried out for a droplet-laden, homogeneous turbulent flow over an unheated and heated cylinder, and body-centered cubic arrangement of spheres. Droplets were observed to impact the cylinder surface and either wet (leading to dripping) or rebound off the surface. Coating of an obstacle surface by a liquid agent, as opposed to gaseous agents, may be considered a positive event in that the agent will cool the surface and inhibit reignition. The body-centered cube results indicated that it takes a relatively high blockage ratio to influence significantly liquid agent transport past an obstacle and prevent the transport of agent to a flame. Comparison of the velocity fields obtained with and without water droplets indicated that droplet dispersion around an obstacle is dependent on the droplet size and velocity.

Velocity results for the droplet-laden airflow and the droplet-only cases indicated that the airflow is relatively unaffected by heating of the cylinder, while the heat has a significant effect on droplet transport. By considering planar streamlines generated from the droplet velocities upstream of the cylinder, it was possible to construct a dividing streamline that marked the boundary between the spray that impacts the cylinder and the spray that is transported past the cylinder. The lower cross-stream velocities measured for the heated cylinder indicated that a larger core region from the spray was not redirected past the cylinder, and resulted in less droplet transport, especially smaller droplets, into the wake region.

Heating of the cylinder surface resulted in vaporization of impinging droplets, and a visible vapor layer downstream of the cylinder in the shear region. Semi-quantitative sizing of droplets using the peak half-width information of the PIV cross-correlation calculation indicated that droplets are entrained in the wake region, and these droplets are, in general, smaller than those existing in the spray upstream of the cylinder and in the shear layer.

Assuming a positive correlation between droplet size and velocity, larger droplets move ballistically and smaller

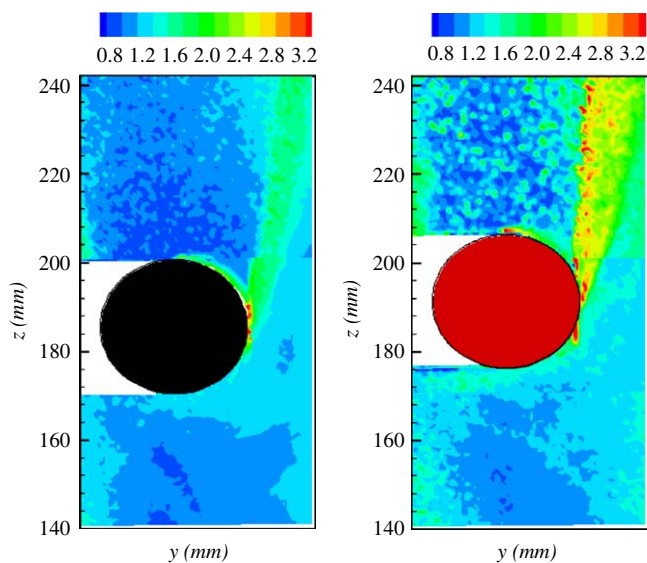


Fig. 27. Relative cross-correlation peak half-widths for spray flow around the unheated (left) and heated (right) cylinders.

droplets are entrained into the surrounding aerodynamic flow field. Thus, different strategies to control and optimize the spatial dispersion of droplets can be developed by including a wide range of droplet sizes, e.g. to disperse droplets far downstream of and/or immediately behind an obstacle. The atomizer design must also be considered since it dictates the initial spatial dispersion of droplets. These points are important for consideration in the development of fire suppression models and validated simulations. In addition, the effect of various spray characteristics like droplet size, velocity, and spatial distribution on transport and extinguishment of fires is important in developing different scenarios for fire suppression.

### Acknowledgements

The authors wish to acknowledge the partial support of this research by the Department of Defense Next Generation Fire Suppression Technology Program, funded by the DoD Strategic Environmental Research and Development Program. The authors wish to thank P. DesJardin, L. Gritzo, D. Keyser, P. Disimile, and J. Tucker for the discussions and guidance that was provided us, B.S. Johnson for help with processing of the PIV data, and R. Fink for his assistance in completing the NIST facility modifications.

### References

- [1] Andersson P, Holmstedt G. Limitations of water mist as a total flooding agent. *J Fire Prot Eng* 1999;4:31–50.
- [2] Dolinar J, Hudgins D, Keyser D, F-18 E/F nacelle simulator input/output boundary condition flows, Report Number A176214 (INS/F-18-1), Naval Air Warfare Center (NAVAIR), October 16, 2002.
- [3] Yoon SS, DesJardin PE, Presser C, Hewson JC, Avedisian CT. Numerical modeling and experimental measurements of water spray impact and transport over a cylinder. *Int J Multiphase Flow* 2006;32: 132–57.
- [4] Chandra S, Avedisian CT. On the collision of a droplet with a solid surface. *Proc R Soc London A* 1991;432:13–41.
- [5] Pasandideh-Fard M, Bussmann M, Chandra S, Mostaghimi J. Simulating droplet impact on a substrate of arbitrary shape. *Atomization Sprays* 2001;11:397–414.
- [6] Hung LS, Yao SC. Experimental investigation of the impaction of water droplets on cylindrical objects. *Int J Multiphase Flow* 1999;25: 1545–59.
- [7] Hung LS. Investigations of the transport and dynamics of droplets impacting on complex objects. PhD dissertation, Department of Mechanical Engineering, Carnegie Mellon University, Pittsburgh, PA, 1998.
- [8] Gonzales JE, Black WZ. Study of droplet sprays prior to impact on a heated horizontal surface. *J Heat Transfer* 1997;119:279–87.
- [9] Yao SC. Dynamics and heat transfer on impacting sprays. In: Tien CL, editor. *Annual Review of Heat Transfer*, vol. 5. Boca Raton, FL: CRC Press; 1994 [Chapter 8].
- [10] Tropea C, Roisman IV. Modeling of spray impact on solid surfaces. *Atomization Sprays* 2000;10(3–5):387–408.
- [11] Crowe CT, Chung JN, Trout TR. Particle mixing in free shear flows. *Prog Energy Combust Sci* 1988;14:171–94.
- [12] Lazaro BJ, Lasheras JC. Particle entrainment and turbulent mixing in free, shear-flows: part 1. The naturally developing mixing layer. *J Fluid Mech* 1992;235:143–78.
- [13] Palero V, Sato K, Ikeda Y, Nakajima T, Shakal J. Stereoscopic particle image velocimetry evaluation in a spray, 8th International Conference on Liquid Atomization and Spray Systems, Pasadena, CA, July 2000, p. 893–900.
- [14] Widmann JF, Presser C. A benchmark experimental database for multiphase combustion model input and validation. *Combust Flame* 2002;129(1/2):47–86 [An erratum is published in 2002; 130 (4): 386–90].
- [15] Tsushima S, Negoro M, Saitoh H, Fuchihata M, Akamatsu F, Katsuki M. Measurement of instantaneous 2-D velocity field and local chemiluminescence in a premixed-spray flame by PIV and MICRO system. 10th International Symposium on the Application of Laser Techniques to Fluid Mechanics, Lisbon, Portugal, July 2000.
- [16] Driscoll KD, Sick V, Gray C. A dual-PIV approach to two-phase flow measurements in fuel sprays. 16th Annual Conference on Liquid Atomization and Spray Systems, Monterey, CA, May 2003.
- [17] Auriemma M, Caputo G, Valentino G, Zarinchang J. Fluid dynamics investigation of fuel spray for SIDI engines by particle image velocimetry. 9th International Conference on Liquid Atomization and Spray Systems, Paper no. 14–34, Sorrento, Italy, July 2003.
- [18] Josefsson G, Fischer J, Magnusson I. Length scale measurements in an engine using PIV and comparison with LDV. 5th International Symposium on Diagnostics and Modeling of Combustion in Internal Combustion Engines, Nagoya, Japan, July 2001.
- [19] Cao ZM, Nishino K, Mizuno S, Torii K. Spray structure and associated droplet velocity in the initial stage of diesel fuel injection. *JSME Int J Ser B* 2000;43:582–9.
- [20] Ikeda Y, Yamada N, Nakajima T. Multi-intensity-layer particle image velocimetry for spray measurement. *Meas Sci Technol* 2000;11: 617–26.
- [21] Gorman S, Widmann JF. An investigation of multiphase particle image velocimetry using Monte Carlo simulations. *Atomization Sprays* 2004;14:525–43.
- [22] Widmann JF, Sheppard DT, Lueptow RM. Non-intrusive measurements in fire sprinkler sprays. *Fire Technol* 2001;37(4):297–315.
- [23] Sheppard DT, Gandhi PD, Lueptow RM. Predicting sprinkler water distribution using particle image velocimetry. 4th Fire Suppression and Detection Research Application Symposium—Research and Practice: Bridging the Gap, Fire Protection Research Foundation, Orlando, FL, February 2000, p. 354–64.
- [24] Sheppard DT, Widmann JF, Lueptow RM. Non-intrusive measurements in fire sprinkler sprays using phase doppler interferometry and particle image velocimetry. 5th Fire Suppression and Detection Research Application Symposium—Research and Practice: Bridging the Gap, Fire Protection Research Foundation, Orlando, FL, February 2001.
- [25] McGrattan KB, Baum HR, Rehm RG. Large eddy simulations of smoke movement. *Fire Safety J* 1998;30:161–78.
- [26] Sheppard DT, Lueptow RM. Measuring and calculating sprinkler water distribution. 6th Fire Suppression and Detection Research Application Symposium—Research and Practice: Bridging the Gap, Fire Protection Research Foundation, Orlando, FL, February 2002, p. 24–32.
- [27] Sheppard DT. Spray characteristics of fire sprinklers. PhD dissertation, Northwestern University, Evanston, IL, June 2002.
- [28] Taylor BN, Kuyatt CE. Guidelines for evaluating and expressing the uncertainty of NIST measurement results. NIST Technical Note 1297, National Institute of Standards and Technology, Gaithersburg, MD, 1994.
- [29] Presser C, Avedisian CT. Transport of high boiling-point fire suppressants in a droplet-laden homogeneous turbulent flow past a cylinder. *Atomization Sprays* 2006;16:627–56.
- [30] Flowmap<sup>®</sup> 3D-PIV System Owner's Manual. Dantec Measurement Technology, Inc., Mahwah, NJ, July 1999.
- [31] Høst-Madsen A, McCluskey DR. On the accuracy and reliability of PIV measurements. 7th International Symposium on the Application of Laser Techniques to Fluid Mechanics, Lisbon, Portugal, July 1994.

- [32] McCluskey DR. Obtaining high-resolution PIV vector maps in real-time. International Workshop on PIV, Fukui, Japan, July 1995.
- [33] Arik EB, Carr J. Digital particle image velocimetry system for real-time wind tunnel measurements. 17th International Congress on Instrumentation in Aerospace Simulation Facilities, 1996. p. 267–77.
- [34] Willert CE, Gharib M. Digital particle image velocimetry. *Exp Fluids* 1991;10:181–93.
- [35] High-accuracy module for flowmanager, Dantec Dynamics Product Information (Pi 740201), 2001.
- [36] Prasad AK, Jensen K. Scheimpflug stereocamera for particle image velocimetry in liquid flows. *Appl Opt* 1995;34(30):7092–9.
- [37] Morck T, Mengel F, Madsen B. 3D-PIV Measurements in an automotive scale wind tunnel. 3rd International Workshop on Particle Image Velocimetry, Santa Barbara, September 1999.
- [38] Wang G, Bachalo EJ, Sankar SV, Bachalo WD. An investigation of spray interaction with large-scale eddies. 5th Annual Conference on Liquid Atomization and Spray Systems (ILASS Americas '92), San Ramon, CA, 1992. p. 53–8.
- [39] van Dyke M. An album of fluid motion. Stanford, CA: Parabolic Press; 1982. p. 88–9.
- [40] Adrian RJ. Limiting resolution of particle image velocimetry for turbulent flow. *Advances in turbulence research*, Postech, Pohang, Korea, 1995. p. 1–19.
- [41] Williamson CHK. Oblique and parallel modes of vortex shedding in the wake of a circular cylinder at low Reynolds numbers. *J Fluid Mech* 1989;206:579–627.
- [42] Meinhart CD, Wereley ST, Santiago JG. A PIV algorithm for estimating time-averaged velocity fields. *J Fluids Eng* 2000;122:285–9.